Characterization and Control of Non-stoichiometry in $Pr_{0.1}Ce_{0.9}O_{2-\delta}$ thin films: Correlation with SOFC Electrode Performance

by

Di Chen

B.S. Materials Science and Engineering
Tsinghua University, 2008

SUBMITTED TO THE DEPARTMENT OF MATERIALS SCIENCE AND ENGINEERING
IN PARTIAL FULFILLMENT OF THE REQUIREMENTS FOR THE DEGREE OF

DOCTOR OF PHILOSOPHY
IN MATERIALS SCIENCE AND ENGINEERING

AT THE
MASSACHUSETTS INSTITUTE OF TECHNOLOGY

June 2014

Signature redacted

Authored by _____
Di Chen
Department of Materials Science and Engineering
May 16, 2014

Signature redacted

Certified _____
Harry L. Tuller
Professor of Ceramics and Electronic Materials
Thesis Supervisor

Signature redacted

Accepted by _____
Gerbrand Ceder
Chair, Departmental Committee on Graduate Students

Characterization and Control of Non-stoichiometry in $Pr_{0.1}Ce_{0.9}O_{2-\delta}$ thin films:

Correlation with SOFC Electrode Performance

By

Di Chen

Submitted to the Department of Materials Science and Engineering

On May 16th, 2014

in Partial Fulfillment of the Requirements for the Degree of

Doctor of Philosophy in Materials Science and Engineering

ABSTRACT

While the properties of functional oxide thin films often depend strongly on oxygen non-stoichiometry (δ), there have been few means available for its measurement and control in a reliable and *in-situ* fashion. In this work, we investigate means for extracting the oxygen non-stoichiometry of dense oxide thin films as a function of temperature and oxygen partial pressure from an analysis of the chemical capacitance (C_{chem}) obtained by impedance spectroscopy, and the use of electrical bias as a means of systematically controlling the non-stoichiometry. We selected the $Pr_xCe_{1-x}O_{2-\delta}$ (PCO) solid solution system as a model system given its mixed ionic-electronic conductivity, well described defect equilibria and transport properties, and stability over with limits of temperature and oxygen partial pressure.

$Pr_xCe_{1-x}O_{2-\delta}$ (PCO) thin films with x=0.01, 0.10 and 0.20 were prepared as thin film cathodes by pulsed laser deposition onto single crystalline $Y_{0.16}Zr_{0.84}O_{1.92}$ electrolyte substrates. The cathode reactions were examined as a function of electrode geometry, temperature, oxygen partial pressure by means of electrochemical impedance spectroscopy (EIS). A DC bias range of ΔE = -100 mV to 100 mV was used to polarize the PCO films and examine the impact on area specific resistance (*ASR*) and film non-stoichiometry. The PCO cathodes exhibited typical mixed ionic electronic behavior including large chemical capacitance and electrode performance, as reflected in the magnitude of the *ASR*, found to be limited by surface oxygen exchange kinetics.

With the aid of a defect equilibrium model, expressions relating chemical capacitance directly to non-stoichiometry, without need for fitting parameters, were derived. By examining the dependence of non-stoichiometry on temperature and pO_2, the thermodynamic constants defining defect generation were extracted. While general agreement of these constants with bulk values derived by thermogravimetric analysis was found, confirming the suitability of using C_{chem} to measure oxygen non-stoichiometry of thin oxide films, the films were found to reduce somewhat

more readily than bulk PCO. Potential sources of error observed in earlier C_{chem} studies on perovskite structured oxide films are also discussed.

When a DC bias was applied, the non-stoichiometry of the PCO films calculated from the measured C_{chem} agreed well with predicted values assuming that the effective change in oxygen activity, $pO_{2,\ effective}$ corresponded to the value expected based on the applied Nernst potential. These results confirm the suitability of using bias across an electrochemical cell to conveniently and precisely control δ of oxide thin films in an in-situ fashion. Of further interest was the ability to readily reach oxygen activities equivalent to pO_2s as high as 280 atm.

Calculated values for the surface exchange coefficient, k, were found to be comparable in magnitude to those exhibited by other popular mixed ionic electronic conductors, therefore confirming the suitability of PCO as a model mixed conducting cathode material. Interestingly, the magnitude of k was found to be largely dependent on the non-stoichiometry in the PCO films, rather than the oxygen activity in the gas phase, at all temperatures studied. This indicates the important role that defects (electronic defect and oxygen vacancy) play in the cathode reaction.

Thesis Supervisor: Harry L. Tuller

Title: Professor of Ceramics and Electronic Materials

Contents

LIST OF PUBLICATIONONS

1. D. Chen, H. L. Tuller, The corellation between oxygen non-stoichiometry and oxygen exchange rate. *in preparation.*

2. D. Chen et al., Conductivity and conductivity relaxation of $Ce_{0.8}Zr_{0.2}O_{2-\delta}$, *in preparation.*

3. D. Chen, S. R. Bishop, H. L. Tuller, Non-stoichiometry in oxide thin films operating under anodic conditions, *in preparation.*

4. D. Chen, H. L. Tuller, The bias effects on the oxygen activity of oxide thin films, *in preparation.*

5. S. R. Bishop, D. Chen, J. Sheth, S.T. Misture, B.W. Sheldon, J. J. Kim, and H. L.Tuller, Impact of size scale on electro-chemo-mechanical coupling properties in MIECs: Bulk and thin film $(Pr,Ce)O_{2-\delta}$. *ECS Transactions, accepted* (2014)

6. Y. Zhang, J.J. Kim, D. Chen, H L. Tuller, G. Rutledge, Electrospun polyaniline fibers as chemiresistive sensors for ammonia and nitrogen dioxide gases. *Advanced Functional Materials, accepted* (2014).

7. D. Chen, A. Groß, D. C. Bono, J. Kita, R. Moos, H. L. Tuller, Electrical conductivity relaxation measurements: application of low thermal mass heater stick. *Solid State Ionics, accepted* (2014).

8. J.L.M. Rupp, E. Fabbri, D. Marrocchelli, J.-W. Han, D. Chen, E. Traversa, H.L. Tuller, B. Yildiz, Scalable oxygen-ion transport kinetics in metal-oxide films: Impact of thermally induced lattice compaction in acceptor doped ceria films. *Advanced Functional Materials, accepted* (2014).

9. J.G. Swallow, W.H. Woodford, Y. Chen, Q. Lu, J.J. Kim, D. Chen, Y.-M. Chiang, W. C. Carter, B. Yildiz, H. L. Tuller, and K.J. Van Vliet, Chemomechanics of ionically conductive ceramics for electrical energy conversion and Storage. *Journal of Electroceramics, accepted* (2014).

10. F. Gao, D. Chen, H. L. Tuller, C. V. Thompson, T. Palacios, On the redox origin of surface trapping in AlGaN/GaN HEMTs, *Journal of Applied Physics* **115**, 124506 (2014)

11. M. N. Luckyanova, D. Chen, W. Ma, H. L. Tuller, G. Chen, B. Yildiz, Control of thermal conductivity by annealing of reducible oxides – the case of $Pr_{0.1}Ce_{0.9}O_{2-\delta}$ thin films, *Applied Physics Letter* **104**, 061911 (2014).

12. J. J. Kim, S. R. Bishop, N. Thompson, D. Chen, H. L. Tuller, Investigation of non-stoichiometry in oxide thin films by simultaneous in situ optical absorption and chemical capacitance measurement: Pr doped ceria – case study. *Chemistry of Materilas* **26**, 1374-1379 (2014).

13. D. Chen, S. R. Bishop, H. L. Tuller, Non-stoichiometry in oxide thin films operating under anodic conditions: a chemical capacitance study of the Praseodymium-Cerium oxide system. *ECS Transactions* **57**, 1387 (2013).

14. D. Chen, S. R. Bishop, H. L. Tuller, Non-stoichiometry in oxide thin films: a chemical capacitance study of the Praseodymium-Cerium oxide system. *Advanced Functional Materials* **23**, 2168 (2013).

15. D. Chen, S. Bishop, H. Tuller, Praseodymium-Cerium oxide thin film cathodes: study of oxygen reduction reaction kinetics. *Journal of Electroceramics* **28**, 62 (2012).

16. F. Gao, D. Chen, B. Lu, H. Tuller, C. V. Thompson, K. Stacia, U. K. Mishra, and T. Palacios, Impact of moisture and fluorocarbon passivation on the current collapse of AlGaN/GaN HEMTs. *IEEE Electron Device Letters* **33**, 1378 (2012).

17. H. L. Tuller, S. R. Bishop, D. Chen, Y. Kuru, J.-J. Kim, and T. S. Stefanik, Praseodymium doped ceria: Model mixed ionic electronic conductor with coupled electrical, optical, mechanical and chemical properties. *Solid State Ionics* **225**, 194 (2012).

18. Y. Kuru, D. Marrocchelli, S. Bishop, D. Chen, B. Yildiz, and H. L. Tuller, Anomalous chemical expansion behavior of $Pr_{0.2}Ce_{0.8}O_{2-\delta}$ thin films grown by pulsed laser deposition. *Journal of the Electrochemical Society* **159**, F799 (2012).

19. S. R. Bishop, D. Chen, Y. Kuru, J. J. Kim, T. S. Stefanik, H. L. Tuller, Measurement and modeling of electrical, mechanical, and chemical properties of a model mixed ionic electronic conductor: Pr doped Ceria. *ECS Transactions* **33**, 51 (2011).

20. S. R. Bishop, J. J. Kim, N. Thompson, D. Chen, Y. Kuru, T. S. Stefanik, and H. L. Tuller, Mechanical, electrical, and optical properties of $(Pr,Ce)O_2$ solid solutions: kinetic studies. *ECS Transactions* **35**, 1137 (2011).

PATENT

1. F. Gao, D. Chen, B. Lu, T. Palacios, Passivation technique for wide bandgap semiconductor devices, International Patent No. WO: 2013/163137, (2012)

LIST OF FIGURES

LIST OF TABLES

ACKNOWLEDGEMENTS

In working towards my Ph.D there have been many individuals who have assisted me. Without their support this thesis would not have been possible.

First and foremost, I would like to thank my doctoral advisor, Professor Harry Tuller, for guiding me through my entire academic and research work over the past six years. He has been a very patient mentor and extremely supportive teacher. I am truly grateful to have been a member of his research group. I would also like to thank my Thesis Committee, Professor Geoffrey Beach, Professor Bilge Yildiz, and Prof. Maria Flytzani-Stephanopoulos for their critical questioning and comments that helped improve my thesis.

I would like to thank Prof. Sean Bishop, Jae Jin Kim, Andreal Groß, David Bono, Prof. Ralf Moos, Maria N. Luckyanova, Wen Ma, Prof. Gang Chen, Prof. Yener Kuru, Dario Marrocchelli, Prof. Jennier Rupp, Jay Sheth, Prof. Scott .T. Misture, Prof. Brian.W. Sheldon, Feng Gao, Prof. Carl V. Thompson, Prof. Tomás Palacios, Yuxi Zhang, Prof. Gregory C. Rutledge, Yidan Cao for the close collaboration in the various projects. Some of their ideas, techniques, and results contributed towards piecing together my thesis. I am also indebted to them for the critical discussion and analysis.

Many thanks go to the graduate students, post-docs, and visiting scientists of the Tuller group. As colleagues and friends, they taught me many important technical skills, helped me navigate the ups and downs of research, and were always around for lively discussions. Thanks to this group of people, my time at MIT was very enriching: Johanna Engel, Nicholas Thompson, Kiran Adepalli, Stuart N. Cook, Nicola Perry, and Michael Campion. Especially, I would also thank the help of former students WooChul Jung, Scott Litzelman, Kengo Haga and George Whitfield. I am really grateful to them for advising and even babysitting me when I first joined the group.

I would also like to give my thanks to my friends from MIT Economics and Talent Forum and Consulting Club at MIT, although I cannot name them one by one. I have unforgettable memories of time here with them.

Above all, I would like to express my respect, love, and thanks to my father Congzhi Chen, my mother Yuanju Pi, and other family members. Their support and love have been ceaseless, tireless, and too often thankless. I certainly would have never made it this far without their support.

April 21th, 2014

Di Chen

1. CHAPTER 1 INTRODUCTION

1.1. Motivation

Deviations from stoichiometry are common in transition metal and rare earth oxides and are generally associated with changes in the oxidation states of the respective cations. Well known examples include $TiO_{2-\delta}$, $Fe_{3-\delta}O_4$, $SrTi_{1-x}Fe_xO_{3-\delta}$ and $CeO_{2-\delta}$, where δ is a measure of the level of non-stoichiometry exhibited by the material under given conditions of temperature and partial pressure of oxygen, pO_2 [1][2][3][4]. Many physical and chemical properties are often strong functions of δ including electrical conductivity[5], magnetic permeability[6], optical absorptivity and luminescence[7], oxygen and cation diffusivities[8], thermal conductivity[9,10] etc.

Oxides, in the form of thin films, nanoparticles, or nanowires are rapidly taking on critical technological functions in various fields including for example memristor [11] and magneto-optic based memories[12], dye sensitized solar cells[13], chemical sensors[14], micro-batteries[15] and micro-fuel cells[16], just to name a few. Additionally, the ability to reproducibly prepare films with well-defined microstructure, thickness, orientation, crystallinity [17], and composition has enabled a more careful and systematic investigation of their transport properties [18,19]. Even with the critical role that the extent of non-stoichiometry plays in controlling the properties of these oxide films, in surprisingly few cases is δ of these oxides known, or how best to control it. First, methods for measuring non-stoichiometry *in-situ* are needed to enable one to correlate changes in δ with changes in annealing conditions. While this can be readily done with bulk specimens – TGA or electrical conductivity in combination with knowledge of mobilities [20], it is difficult to do so in films, because of the very small mass changes involved. Furthermore, it is often difficult to access certain experimental conditions, e.g. at sufficiently high temperatures or extremes in partial or total pressure of oxygen [21–23]. Likewise, it is often difficult to change δ by

small increments, particularly important if one is close to a phase transition or where properties are sharp functions of pO_2 as in the $VO_{2\pm\delta}$ system [24].

The most widely used technique to control oxygen stoichiometry is by varying the pO_2. Bias, on the other hand, could be expected to be a fast and convenient way to control the oxygen stoichiometry. While some researchers have tried to use bias to control the oxygen stoichiometry, to our knowledge, few studies have been able to simultaneously measure and control the non-stoichiometry of films accurately. For example, In Ref. [25] [26], the oxygen stoichiometry is not measured. In Ref. [27], the oxygen stoichiometry is measured but doesn't fit the predicted defect model. For example, Backhaus-Ricoult et al. and Chen et al. used bias to control the oxygen stoichiometry of $La_xSr_{1-x}MnO_{3-\delta}$, but the oxygen stoichiometry is not measured. [25] [26] Kawada et al. measured the non-stoichiometry of $La_{0.6}Sr_{0.4}CoO_{3-\delta}$ using chemical capacitance, C_{chem}, and attempted to control it using bias, but δ turned out to be much smaller than that measured in bulk specimens of the same composition. Others following a similar approach found just the opposite behavior with the films exhibiting a larger non-stoichiometry than bulk specimens. [27][28]

What is needed is a technique able to precisely measure and control, *in-situ*, the oxygen non-stoichiometry of oxide thin films. In this study, we demonstrate the feasibility of both monitoring and controlling the oxygen stoichiometry of $Pr_{0.1}Ce_{0.9}O_{2-\delta}$ (PCO) thin films. We then demonstrate that this technique could be a powerful tool for studying and identifying the rate determining step controlling the cathode reaction in Solid Oxide Fuel Cells (SOFCs).

1.2. Surface reactions at SOFC cathodes

1.2.1. Solid Oxide Fuel Cell (SOFC)

The world is currently heavily dependent on fossil fuels for energy. Approximately 80 to 90 percent of world energy consumption is derived from the combustion of fossil fuels [29]. The dependence on fossil fuels is having a grave impact on the environment, because it generates greenhouse gas emissions and potentially contributes to a global environmental catastrophe. As a consequence, clean energy conversion devices, such as fuel cells, have received much attention in recent years. Fuel cells are electrochemically energy conversion systems that convert the chemical energy stored in fuels directly into electricity, without involving the process of combustion [30].

The fundamental building block of a fuel cell is shown in **Figure 1.1**. It consists of two electrodes separated by an electrolyte (or membrane). The electrolyte serves as a barrier to gas diffusion, but allows ions to migrate across it. Accordingly, half-cell reactions occuring at the anode and cathode, produce ions which can traverse the electrolyte, while electrons are required to travel through the external load [31]. This is how the fuel cell creates the electricity. Since it doesn't rely on the heat of combustion, the fuel cell, in principle, provides superior potential efficiency with significantly reduced emissions of pollutants, compared with conventional combustion processes such as an automotive engine or an electrical power station. In addition to high efficiency and low emissions, fuel cells are attractive for their modular and distributed nature, and nearly zero noise pollution [31]. Furthermore, they link hydrogen and electricity, two highly compatible energy carriers that embody the ideals of a sustainable energy economy in the future [32].

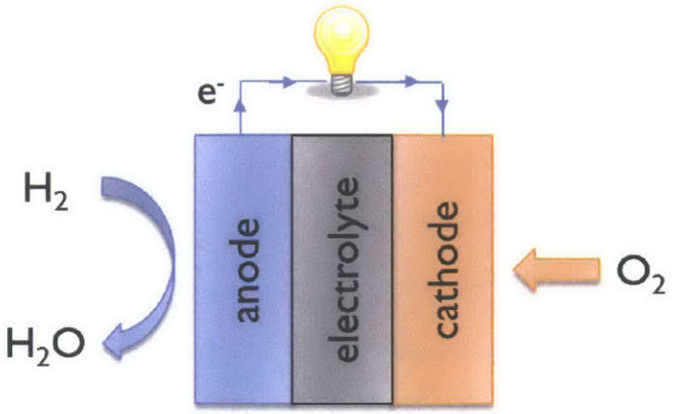

Figure 1.1 Schematic of a fuel cell comprised of an electrolyte, an anode and a cathode. The overall chemical reaction is $H_2 + 1/2O_2 = H_2O$.

There is a range of different fuel cell technologies, each with its own materials set and suited to different applications. The electrolyte can be an acid, base, salt, or a solid ceramic that conducts ions. A fuel cell using a solid metal oxide electrolyte that is conductive to oxygen ions was first reported by Baur and Preis in 1937 [33]. This is now called a solid oxide fuel cell (SOFC). The use of an oxide electrolyte has several distinct advantages over other types of fuel cells in that these materials are chemically, thermally and mechanically stable. This importantly eliminates the corrosive and containment issues associated with liquid electrolytes. In certain modes of operation, SOFCs have demonstrated the longest lifetime of any fuel cell system. For example, a 100-kW system fabricated by Siemens-Westinghouse, successfully produced power for more than 20,000 h, with minimal degradation in performance [34].

The key feature of the SOFC is its high operating temperature. Typical SOFCs operate in the temperature range of 800–1000°C, typified by developers such as Siemens Westinghouse and Rolls-Royce [35]. Such high temperature operation results in fast transport and electrochemical reaction kinetics, thus reducing the irreversible losses that occur in fuel cells due to electrode kinetics and ohmic resistances. Furthermore, the high operating temperature enables the SOFCs

to be used in combined heat and power applications or efficiently coupled with gas turbines [36]. Therefore, high temperature SOFCs generally provide the highest conversion efficiency among the various types of fuel cells, while reducing the catalytic activity requirements of the electrode materials [37]. In addition, at high temperatures, it is easier to break C-C bonds and thus some hydrocarbons can be directly utilized at the anode providing flexibility of fuel choices; from hydrogen to hydrocarbons (especially natural gas) [38].

The high operating temperatures of the SOFCs, however, do contribute to problems related to cost and reliability. For example, more expensive materials need to be used in interconnects and heat exchangers. Also, the high temperatures lead to durability problems associated with thermal cycling and performance degradation because of interdiffusion or reaction between the individual components. High operation temperatures also slow the start-up and shut-down process. Because of those reasons, the focus of SOFC development has been on lowering the operating temperatures.

Operation at lower temperature, however, creates a number of materials problems that are associated with the increase in the electrolyte resistance and decrease in the rates of the electrocatalytic reactions occurring at the electrodes. Both factors result in a reduction of the cell voltage and output power. Therefore, much effort is being focused on: (1) finding alternative electrolyte materials with higher ionic conductivity at low temperatures than conventional yttria stabilized zirconia (YSZ), such as doped ceria and doped lanthanum gallate [31] ; (2) decreasing the YSZ electrolyte thickness based on, for example, MEMS techniques, which have recently been applied towards accommodating very thin-film electrolytes designed to reduce electrolyte resistance [16]; (3) minimization of electrode polarization resistance, especially the cathode polarization resistance. The last one being the focus of this study.

1.2.2. Cathode reactions

The overall reaction at the SOFC cathode can be written as:

$$\frac{1}{2}O_2(gas) + 2e^{'} + V_O^{\bullet\bullet} \rightarrow O_O^{\times} \qquad (1.1)$$

where $V_O^{\bullet\bullet}$ is a doubly positively charged oxygen vacancy, $e^{'}$ is an electron and $O_O^{\times}$ represents an oxygen ion in the cathode or electrolyte lattice. The reaction, though appearing to be simple, can be quite complex and comprises many steps. These steps may involve gas phase diffusion, adsorption, dissociation, electronation, diffusion, and finally incorporation of oxygen into the crystal lattice of the electrolyte, as schematically illustrated in **Figure 1.2**. In general, two limiting classes of pathways are possible, as shown schematically in **Figure 1.3** [39]. The pathway can involve transport across dual-phase boundaries (the 2PB pathway), or it can be largely constricted to the triple-phase boundaries at which the gas and two of the solid phases are in simultaneous contact (the 3PB pathway). For the 2PB pathway to become possible, the electrode needs to be both an ionic conductor and an electronic conductor, or so called mixed ionic electronic conductor (MIEC). Clearly, the 2PB pathway has much more reaction sites than 3PB pathway. That is why there is an explosion of interest in recent years for the use of MIEC materials as cathodes.

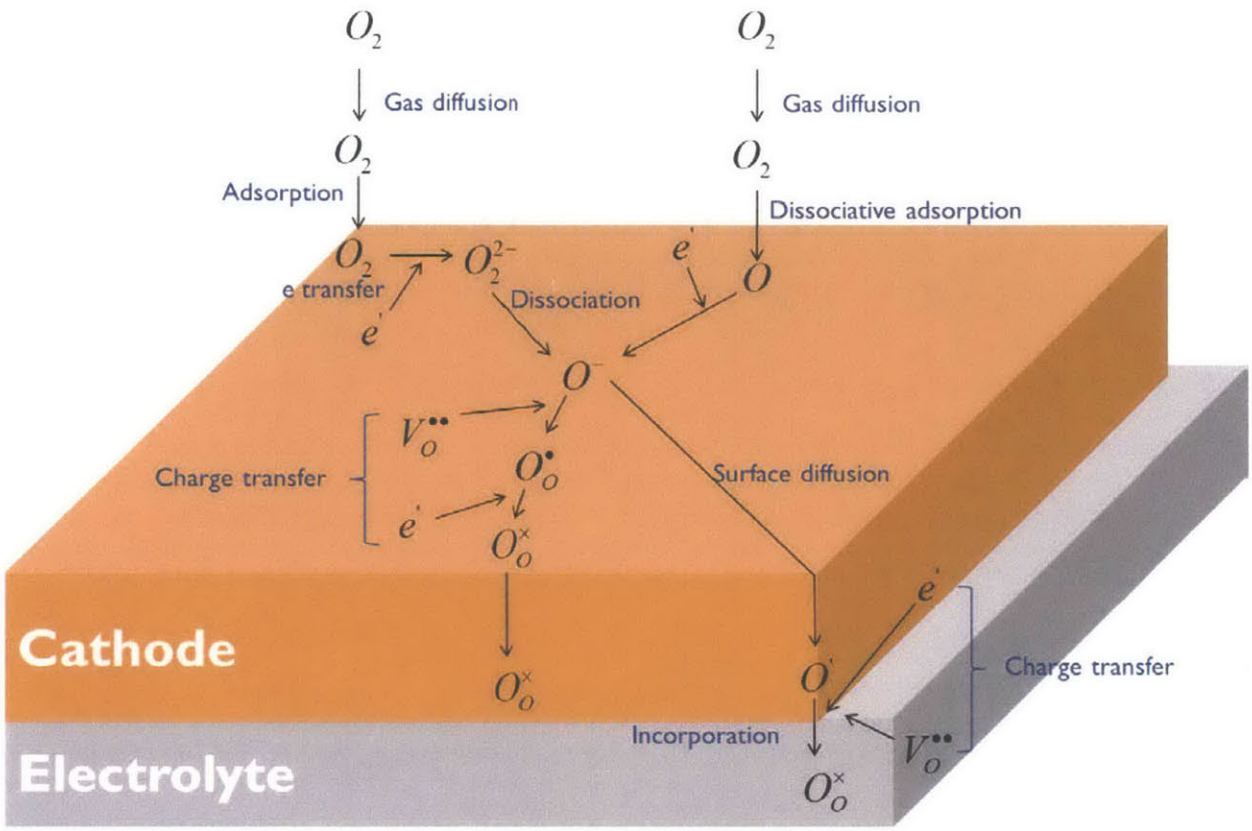

Figure 1.2 Schematic illustration of possible elementary reaction steps during the cathode reaction.

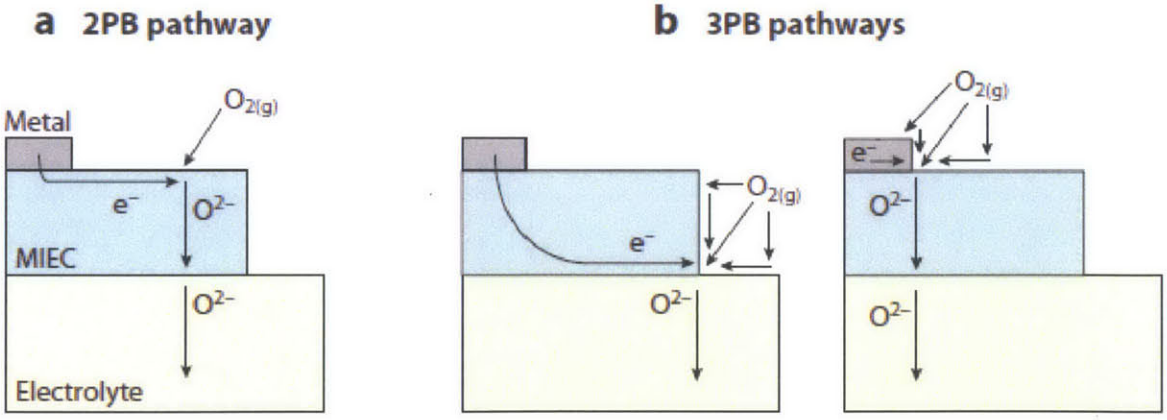

Figure 1.3 Macroscopic reaction pathways involving (a) the dual-phase boundary (2PB) and (b) triple-phase boundaries (3PBs). The oxygen electroreduction reaction is shown as an example. Reprinted from a reference [39].

1.2.3. Rate determine steps (RDS)

As shown in Figure 1.2, the cathode reaction comprises, in principle, many steps. This complexity makes the reaction mechanism still poorly understood. Maier described how to derive atomistic expressions for the surface exchange rate (k*) by applying chemical kinetics to detailed reaction mechanisms[40]. The key assumption of the approach is Bodenstein's principle: one step in the pathway is assumed to be rate determining and all pre- and succeeding reaction steps are treated as being at quasi-equilibrium. The rate of the overall process is consequently given by the rate of the determining step (RDS). By comparing experimental and theoretical dependences of k* on thermodynamic variables such as activity of the reactant species (i.e., oxygen partial pressure, vacancy concentration, hole concentration, electron concentration) and temperature, one can infer possible reaction mechanisms. Some examples are listed below.

Merkle and coworkers, using optical relaxation spectroscopy measurement as a function of pO_2 in single crystal Fe doped $SrTiO_3$ model systems (perovskite mixed conducting electrodes), suggested a detailed mechanistic pathway and concluded that the RDS is either the transfer of one of the very few conduction band electrons e' to form adsorbed peroxide species, or the bond dissociation of $O_{2,ad}^{2-}$ [41]. By reviewing a large number of data sets obtained from various acceptor-doped fluorites and perovskites (including CeO_2, LSGM, STF, LSCF and doped $CaZrO_3$), De Souza suggested the availability of electronic species determines the rate of oxygen exchange [42]. In an electrochemical study of thin-film STF deposited on YSZ, Jung and Tuller found that, under oxidizing conditions ($pO_2 > 10^{-2}$ atm), the activation energy of the exchange rate constant was close to that of the bulk activation energy for generating electronic defects by thermal excitation [$k_0 \propto a_{e'_s}$, i.e., $E = E_C - E_F$], over a remarkably wide range of activation energies (1.5 to 2.5 eV)[43]. On this basis, they concluded that the minority electronic defects

must be involved in the electrochemical reaction pathway and further speculated that a one-electron transfer to adsorbed oxygen may be the RDS.

Nearly every conceivable rate limiting step has been suggested so far. However, a general agreement with respect to the reaction mechanism has, in most cases, not yet been achieved. In Chueh and Haile's review paper[39], they showed the exchange rate constant depends directly on the equilibrium reactant and product concentration in the RDS, which , in the general case, are reaction intermediates. Thus, the task becomes that of relating the concentrations of these intermediates to those of the global reactants and products (in the case of oxygen electroreduction, gaseous oxygen, electrons, and oxygen vacancies, as shown in Figure 1.2). For a given global reactant/product under consideration, one needs to know only the number of species transferred before, during, or after the RDS, and the number of times such reaction needs to proceed in the net reaction. With this understanding, they calculated the dependence of exchange rate constant on the activities of global reactants and products (**Tables 1.1, 1.2, and 1.3**).

Table 1.1 The dependence of the oxygen exchange rate constant on the oxygen partial pressure for various situations[a]. Reprinted from reference [39].

O_2(g) adsorbed	Type of oxygen intermediate in the RDS	
	Atomic oxygen	At least one diatomic oxygen
Before RDS	$pO_2^{1/4}$	$pO_2^{1/2}$
During RDS	$pO_2^{1/2}$	$pO_2^{1/2}$

[a]Does not include indirect oxygen partial pressure dependence via oxygen vacancy or electronic defect activities.

Table 1.2 The dependence of the oxygen exchange rate constant on oxygen vacancy activity when the vacancy is transferred before, during, or after the rate-determining step (RDS). Reprinted from reference [39].

Oxygen vacancy transferred	Type of oxygen intermediate in the RDS	
	Atomic oxygen	**At least one diatomic oxygen**
Before RDS	$\sqrt{a_{V_{O,s}^{\bullet\bullet}}}$	$a_{V_{O,s}^{\bullet\bullet}}$
During RDS	$\sqrt{a_{V_{O,s}^{\bullet\bullet}}}$	$a_{V_{O,s}^{\bullet\bullet}}$
After RDS	$\sqrt{a_{V_{O,s}^{\bullet\bullet}}^{-1}}$	$a_{V_{O,s}^{\bullet\bullet}}^{-1}$

Table 1.3 The dependence of oxygen exchange rate constant on electronic defect activity as a function of the number of electrons transferred before and during the rate-determining step (RDS)[a,b]. Reprinted from reference [39].

Number of electronic species transferred during RDS	Number of electronic species transferred before RDS		
	Zero	**One**	**Two**
Zero	$a_{e_s'}^{-1}, \sqrt{a_{e_s'}^{-1}a_{h_s^{\bullet}}}, \sqrt{a_{e_s'}^{-1}a_{h_s^{\bullet}}}, a_{h_s^{\bullet}}$	$0, \sqrt{a_{e_s'}a_{h_s^{\bullet}}}, \sqrt{a_{e_s'}^{-1}a_{h_s^{\bullet}}^{-1}}, 0$	$a_{e_s'}, \sqrt{a_{e_s'}a_{h_s^{\bullet}}^{-1}}, \sqrt{a_{e_s'}a_{h_s^{\bullet}}^{-1}}, a_{h_s^{\bullet}}^{-1}$
One	$0, \sqrt{a_{e_s'}a_{h_s^{\bullet}}}, \sqrt{a_{e_s'}^{-1}a_{h_s^{\bullet}}}, a_{h_s^{\bullet}}$	$a_{e_s'}, \sqrt{a_{e_s'}a_{h_s^{\bullet}}}, \sqrt{a_{e_s'}a_{h_s^{\bullet}}^{-1}}, 0$	-
Two	$a_{e_s'}, \sqrt{a_{e_s'}a_{h_s^{\bullet}}}, \sqrt{a_{e_s'}a_{h_s^{\bullet}}}, a_{h_s^{\bullet}}$	-	-

[a]For reactions involving atomic oxygen species in electron-transfer steps. Four values are indicated for each reaction pathway corresponding to four situations: (*a*) both electronic defects transferred are electrons; (*b*) the first is an

electron and the second is an electron hole; (*c*) the first is a hole and the second is an electron; and (*d*) both are holes. In the dilute limit, the defect activity is equal to the concentration. The general outcome is as follows: Electrons or holes participating in the RDS (either as reactants or products) give an exchange rate constant that depends positively on the electron/hole concentrations. An electron transferred before the RDS or hole transferred after it also yields an exchange rate constant that depends positively on the electron/hole concentration; an electron transferred after the RDS or hole transferred before it gives an exchange rate constant that depends negatively on the electron/hole concentration.

[b]Under isothermal conditions, $\sqrt{a_{e_s'} a_{h_s^\bullet}}$ is a constant.

However, to obtain the overall oxygen partial pressure dependence of the exchange rate constant, we must also examine the indirect contributions from electronic defect and oxygen vacancy activities. This is not easy because the electronic defect and oxygen vacancy activities are also impacted by the oxygen partial pressure. In this study, for the first time, we demonstrated that we can control oxygen partial pressure and electronic defect and oxygen vacancy activities separately.

1.3. PCO System

In this study, praseodymium-cerium oxide ($Pr_xCe_{1-x}O_{2-\delta}$; PCO) was selected as the material system, given its surprisingly high degree of flexibility in tuning the non-stoichiometry even under oxidizing (e.g. air) conditions, and its well characterized defect chemistry and electrical properties in the bulk.

Cerium oxide has long been studied as an oxygen ion conducting solid electrolyte material. Typically acceptors (such as Gd^{3+}, Y^{3+}, Sm^{3+}, Ca^{2+}, etc) are added in order to increase the concentration of oxygen vacancies in the system and suppress the electronic conductivity, resulting in an ionic conductor. The solid solubility for such acceptors is quite high in the

fluorite-like CeO_2 structure, giving the opportunity for heavily doped systems (>40%)[44][45]. Doping with a multi-valent cation such as praseodymium can yield a MIEC instead of an ionic conductor. By varying the Pr to Ce ratio, it is possible to control the degree of electronic vs. ionic conductivity over a wide range of pO_2 values and temperatures[46]. Such mixed conductors have applications as fuel cell electrodes[47][48][49][50], oxygen separation membranes[51][52], and surface-effect gas sensors [53]. In addition, the wide range of solid solubility between CeO_2 and Pr_6O_{11}[51][54][55], the large non-stoichiometry possible in the system[56], and the dependence of non-stoichiometry on temperature and pO_2 result in a high degree of flexibility in tuning the non-stoichiometry of the material over a wide pO_2 and temperature range. Furthermore, few systems exist in which a large concentration of a multi-valent cation can be incorporated into a stable, well-studied host material without significantly altering the host material itself.

The defect chemistry and transport model of bulk PCO have been studied by a variety of experimental techniques, including electrical conductivity/ Electrochemical Impedance Spectroscopy (EIS)[20][57], thermogravimetri analysis (TGA)[20][56][58], dilatometry[59], high temperature X-ray diffraction (XRD)[60], and optical spectroscopy[7]; many in this research group. Some of the key findings are summarized below.

The oxygen non-stoichiometry (δ) measured by TGA as a function of pO_2 for PCO20 is shown in **Figure 1.4**. The non-stoichiometry exhibits a plateau at intermediate pO_2, with an increase in non-stoichiometry under more reducing conditions and generally a decrease in non-stoichiometry upon more oxidizing conditions. In **Figure 1.5**, the conductivity of PCO for all Pr-containing compositions measured at 700°C shows similar behavior (except for PCO20).

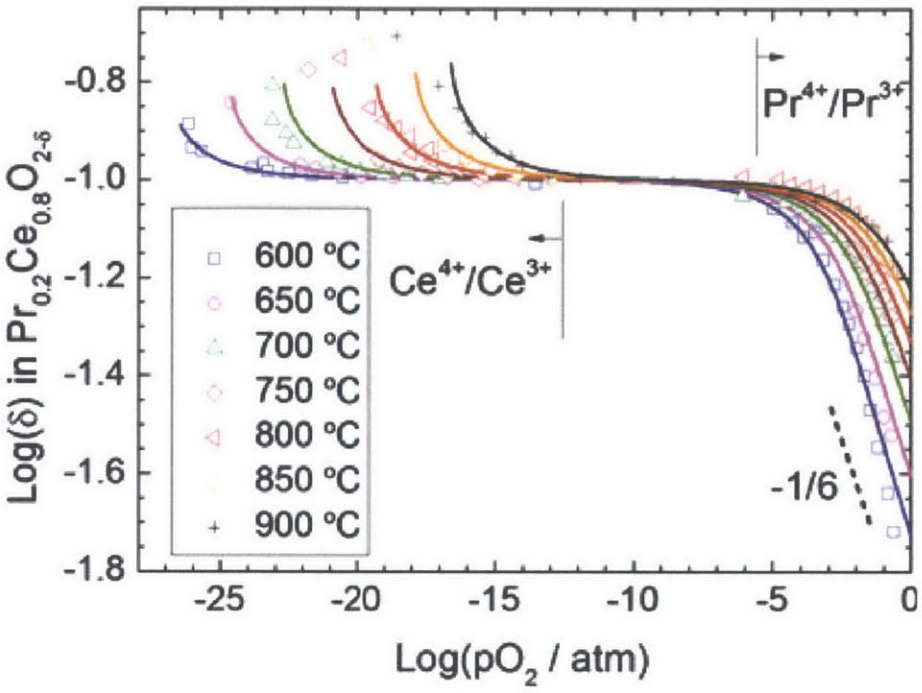

Figure 1.4 Non-stoichiometry of PCO20 (data points) as a function of oxygen partial pressure for a series of isotherms, modeled (solid line) on the basis of the defect chemistry. The characteristic slope for Pr redox and the stoichiometry at which Pr is largely Pr^{4+}. Reprinted from references [61] [58].

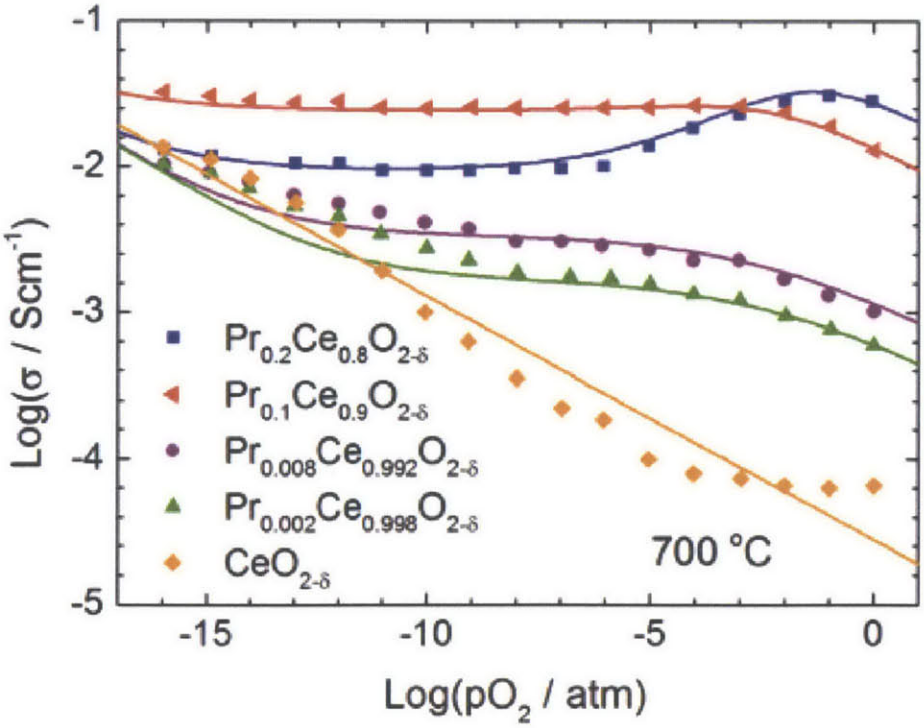

Figure 1.5 Log electrical conductivity versus log pO_2 for a series of compositions in the system $Pr_xCe_{1-x}O_{2-\delta}$ (of x=0, 0.002, 0.008, 0.1, 0.20) measured at 700 °C. Reprinted from a reference [61].

Under highly reducing conditions (low pO_2), the increase in non-stoichiometry and conductivity, is the result of the well-known reduction of Ce^{4+} to Ce^{3+} with the formation of small polarons in the conduction band of ceria (e') and oxygen vacancies through Equation (1.2) .

$$O_O^{\times} \leftrightarrow V_O^{\bullet\bullet} + 2e' + 1/2O_2(g) \qquad (1.2)$$

At intermediate pO_2, Pr is fully reduced (trivalent) and thus acts like an acceptor dopant. The charge neutrality equation is

$$[Pr_{Pr}'] \approx 2[V_O^{\bullet\bullet}] \qquad (1.3)$$

Thereby the oxygen vacancy concentration is fixed. This results in an ionic conductivity independent of pO_2.

As pO_2 is increased, the Pr begins to oxidize back to the 4+ oxidation state, which is isovalent with the Ce host ion. According to Equation (1.3), this state leads to a corresponding decrease in oxygen vacancies. At high pO_2, the electrical conductivity and TGA behavior are consistent with the following reaction:

$$2\,Pr_{Ce}^{\times} + O_O^{\times} \leftrightarrow 2\,Pr_{Ce}' + V_O^{\bullet\bullet} + 1/2O_2(g) \qquad (1.4)$$

In contrast to these expectations, for the highest levels of Pr and particularly for PCO20, the conductivity increases at high pO_2 reaching a maximum before beginning to decrease again. (see Figure 1.5). This is attributed to increasing wave function overlap between adjacent Pr ions with increasing Pr content, thereby broadening the discrete Pr levels within the energy gap of ceria

into impurity bands with the potential to support electron hopping from one ion to the next; the rate of hopping is characterized by the parameters $\mu_{\circ,\mathrm{Pr}_{Ce}}$ and $H_{m,\mathrm{Pr}_{Ce}}$. Because of the localized nature of the electrons within these narrow impurity bands, the so-called small polaron hopping depends on the availability of adjacent empty levels to hop to. In other words, conduction along such bands occurs only if they are partially filled, as reflected by a mixed valent state; i.e., electrons on Pr^{3+} sites can hop only to an adjacent Pr^{4+} site. Thus, the small polaron contribution to the electronic conductivity is proportional to the product of $[\mathrm{Pr}_{\mathrm{Pr}}^{3+}][\mathrm{Pr}_{\mathrm{Pr}}^{4+}]$, leading ideally to a maximum as a function of pO_2 at the point at which the concentrations of the two valence states are equal, revealed by the "maximum" in conductivity at high pO_2 for PCO20.

1.4. Simple and Well-defined Model Structure

1.4.1. Dense thin film

The mechanistic understanding of the electrode reactions still remains unsatisfactory, even though there are numerous studies on the electrochemical properties of different electrode materials. This lack of fundamental knowledge may be related to the fact the vast majority of research done in this field has been performed on complicated electrode morphologies such as porous electrodes [62][63][64][65][66]. The porous electrodes have some advantages for the performance improvement, such as high gas permeability, large surface-to-volume ratio, and especially extended reaction site density at triple phase boundaries (TPB) between electrode, electrolyte and gas phase. However, they usually provide ill-defined structures and geometries, making it difficult to separate, for example, the influence of electrode morphology from the intrinsic properties of the materials. In addition, this complex morphology sometimes comes along with inhomogeneity in surface chemistry, complicating the situation even further.

In recent years, several groups have started to investigate dense thin film cathodes in order to avoid the problems associated with porous systems. These dense thin film electrodes are fabricated by physical vapor deposition (PVD) methods, such as sputtering or pulsed laser deposition. This structure has simple geometry and is quite reproducible. Furthermore, films grown by PVD allow for the control of electrode microstructure more precisely. Features such as crystal orientation, grain size & shape, and compositional variations can be varied by control of deposition conditions, i.e. deposition temperature, pressure, power, gas composition, substrate composition, etc. Finally, this system is sufficiently simple so that it can serve as a good model system represented by a simpler equivalent circuit, allowing for a more reliable interpretation of experimental data.

1.4.2. Pulsed laser deposition

Pulsed laser deposition (PLD) is a thin film deposition (specifically a physical vapor deposition, PVD) technique where a high-power pulsed laser beam is focused inside a vacuum chamber to strike a target of the material that is to be deposited. This material is vaporized from the target (in a plasma plume) which deposits it as a thin film on a substrate (such as a silicon wafer facing the target). This process can occur in ultra high vacuum or in the presence of a background gas, such as oxygen that is commonly used when depositing oxides to fully oxygenate the deposited films.

While the basic-setup is simple relative to many other deposition techniques, the physical phenomena of laser-target interaction and film growth are quite complex. When the laser pulse is absorbed by the target, energy is first converted to electronic excitation and then into thermal, chemical and mechanical energy resulting in evaporation, ablation, plasma formation and even exfoliation [67]. The ejected species expand into the surrounding vacuum in the form of a

plume containing many energetic species including atoms, molecules, electrons, ions, clusters, particulates and molten globules, before depositing on the typically hot substrate. The schematic illustration of the PLD chamber is shown in **Figure 1.6**.[68]

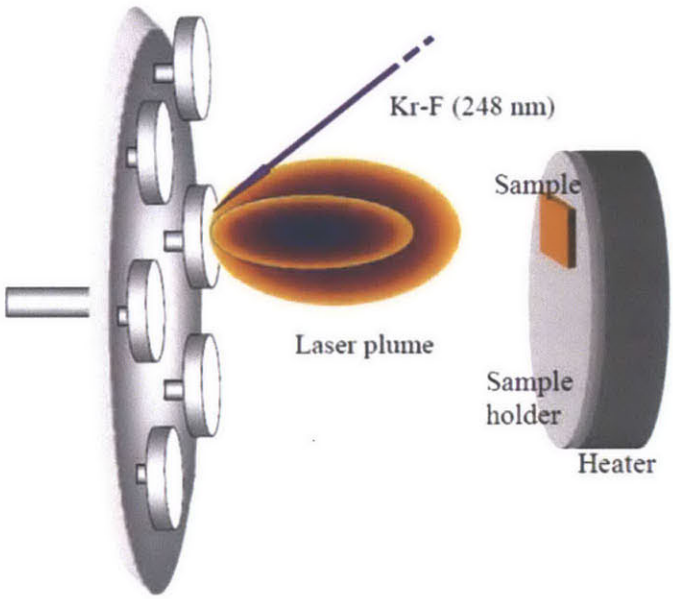

Figure 1.6 Schematic illustration of the PLD chamber[68].

The most desirable aspect of PLD is the ability to largely transfer the stoichiometry of the target material to the sample substrate with essentially little change in chemical composition. This trait is due to the high heating rate of the target surface, approximately 10^8 K/s. At such a high rate, all target constituents effectively evaporate at the same rate, in contrast to other deposition techniques such as sputtering or electron beam evaporation.

1.5. Electrochemical Impedance Spectroscopy (EIS)

Electrochemical impedance spectroscopy (EIS) is a very powerful tool for investigating electrochemical systems. Basic measurements of impedance are typically done by applying a small amplitude, sinusoidal signal and measuring the amplitude and phase of the linear response, as shown in **Figure 1.6**. The experiment is carried over a wide range of frequencies. Impedance

spectroscopy can aid in deconvoluting various processes by examining the electrical response function in the frequency domain, since each contributing process typically has a different time constant [69]. In recent years, EIS has been routinely used in the characterization of coatings, batteries, fuel cells, etc. The potential of impedance spectroscopy in the field of solid state ionics was realized after Bauerle demonstrated in 1969 that the technique can differentiate between bulk, grain boundary and electrode resistances in doped ZrO_2 [70]. Today, impedance spectroscopy is probably the most important tool for investigating electrical transport and electrochemical properties of ionic solids. Well over 7000 papers using this technique appear in the Institute for Scientific Information (ISI) database for the 20-year time period from 1985 to date [71].

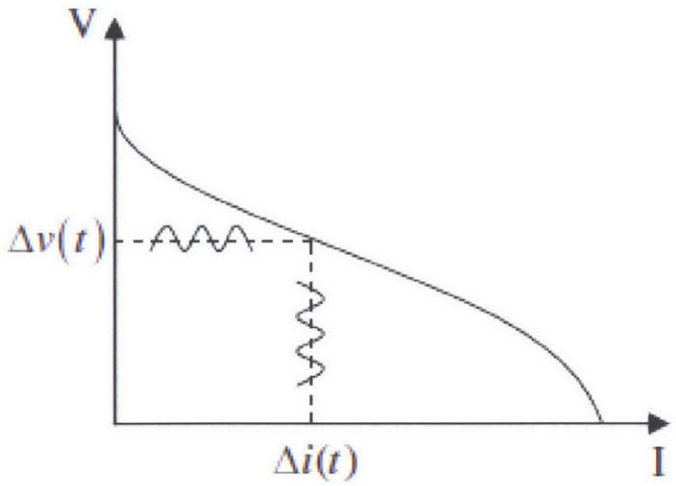

Figure 1.7 Principles of impedance spectroscopy. Reprinted from a reference [72].

Impedance is a generalization of electrical resistance, i.e. $(\boldsymbol{V(\omega)/I(\omega)}$. It is used for periodic signals and accounts for both magnitude and phase information with a complex representation:

$$Z(\omega) = Z' + i \cdot Z'' \tag{1.5}$$

where Z is an impedance vector which depends on the frequency; Z' is the real component of the impedance or resistance; Z'' is the imaginary component of the impedance or reactance; and $i \equiv \sqrt{-1}$.

The most common way to represent impedance data in solid state ionics is by plotting it in the complex impedance plane (imaginary vs. real part of Z, often referred to as Cole-Cole plot). Equivalent circuit representations consisting of resistors, capacitors and other elements are often employed to evaluate and interpret experimental impedance data:

$$\boldsymbol{Z_R(\omega) = R} \tag{1.6}$$

$$Z_C(\omega) = -i\frac{1}{\omega C} \tag{1.7}$$

$$Z_L(\omega) = i\omega L \tag{1.8}$$

where Z_R is the impedance of a resistor, R is resistance, Z_C is the impedance of a capacitor, C is capacitance, Z_L is the impedance of an inductor and L is inductance. These elements can be combined in an infinite variety of series and parallel connections. The net impedance from a combination of two elements with individual impedance depends on whether they are connected in series or parallel, as in the following equations:

$$Z_{Series} = Z_1 + Z_2 \tag{1.9}$$

$$Z_{Parallel} = \frac{1}{\frac{1}{Z_1} + \frac{1}{Z_2}} \tag{1.10}$$

The impedance of combinations of larger numbers of elements can be found by recursively applying these equations. Any arbitrary spectrum, no matter how complicated, can, in principle, be matched by constructing a circuit from individual elements and adjusting the resistances, capacitances, and inductances. More typically, a reasonably approximate fit to experimental data is achieved using as few elements as possible.

1.6. Chemical capacitance (C_{chem})

When an AC signal is applied to the electrode, the oxygen potential in the electrode varies, giving rise to a variation in oxygen vacancy concentration in the electrode. Viewing this from the standpoint of an outer electrical circuit, this behaves as the accumulation or depletion of electrical charge within the electrode. In EIS measurement, a large capacitance is often detected [73]. This capacitance is defined as "chemical capacitance" (C_{chem}) by Jamnik and Maier, to emphasize the connection to a chemical change in the electrode [74].

C_{chem} can be used to represents the storage capacity of oxygen vacancies in a solid. A number of investigators have advanced the use of C_{chem}, in film or bulk form, and related it to the oxygen content of the film using thermodynamic principles. In some cases, the oxygen stoichiometry measured this way does not agree well with that of the bulk, determined by thermogravimetric analysis (TGA) or coulometric titration. This discrepancy is suspected to arise from lattice mismatch stresses in the film or other gas/solid and film/substrate interfacial interactions. For example, a reduced oxygen stoichiometry content has been reported in thin films of $La_{1-x}Sr_xCoO_{3-\delta}$ as compared to the bulk, while others have reported opposite behavior.[27,28,75] At other times, defect formation energies for thin film $Sm_{0.15}Ce_{0.85}O_{2-\delta}$ and oxygen non-stoichiometries for thin film $Gd_{0.1}Ce_{0.9}O_{2-\delta}$ and $La_2NiO_{4+\delta}$ extracted from chemical capacitance

measurements were found to be comparable to bulk values.[76–78] For the CeO_2-based materials, an additional, presumably interfacial, capacitive contribution was observed and an analysis technique was developed to isolate this contribution. In the latter study of $La_2NiO_{4+\delta}$, the results were characterized by a limited data set restricted to only a single pO_2.

In this study, we use C_{chem} to investigate the nonsotichiometry of PCO thin films. The derivation of absolute oxygen vacancy concentration using a relatively simple defect equilibria based analysis is developed, that directly relates chemical capacitance to δ without any fitting parameters. With these absolute values of δ thus evaluated, δ is then determined from chemical capacitance in regions extending away from the simplified defect equilibria approximations. The details of the derivation are presented in Chapter 2.

1.7. Objective

This research has two main objectives. The first is to establish a technique, for the first time, to successfully measure and control the oxygen vacancy concentration of nano-scale oxide thin films. The second is to use this technique to better understand the detailed cathode reactions occurring at PCO electrodes and identifying the rate determining step(s) controlling cathode performance.

2. CHAPTER 2 THEORY

2.1. Defect chemistry of $Pr_{0.1}Ce_{0.9}O_{2-\delta}$

In ceria, oxygen vacancies are introduced in the material through the following defect reactions written in Kröger-Vink notation.

$$O_O^{\times} \leftrightarrow V_O^{\bullet\bullet} + 2e' + 1/2O_2(g) \tag{2.1}$$

where $O_O^{\times}$, $V_O^{\bullet\bullet}$, and e' are oxide ions on oxygen sites, doubly positive charged (with respect to the lattice) oxygen vacancies, and electrons, respectively.

The corresponding mass action relation is

$$\frac{[V_O^{\bullet\bullet}]n^2\, pO_2^{1/2}}{[O_O^{\times}]} = k_r^{\circ} \exp(-\frac{H_r}{kT}) = K_r \tag{2.2}$$

where brackets denote concentration. K_r, H_r, and n are the equilibrium constant, reduction enthalpy of ceria, and electron concentration, respectively.

Oxygen deficientcy also can be induced in ceria by the addion of lower valent substitutents, such as Gd. In this manner, high concentrations of oxygen vacancies can be generated independent of oxygen partial pressure and without the corresponding generation of electrons. One can consider the substituion of dopants whose valence varies with both accessible temperature and pO_2, such as praseodymium (Pr). In this case, one expectes a more complex response. The Pr substitution can lead, at relatively oxidizing conditions, to a pO_2 dependent non-stoichiometry, caused by the reduction of Pr. In a recent paper published by the authors, measurements of oxygen non-stoichiometry and electrical conductivity performed on bulk

$Pr_{0.1}Ce_{0.9}O_{2-\delta}$ (PCO) were presented, and on this basis, a defect equilibrium model was developed.[79]

At high pO_2, electrons in the conduction band can drop down in energy and occupy the deep empty $Pr_{Ce}^{\times}$ trap states through the following reaction

$$e' + Pr_{Ce}^{\times} \leftrightarrow Pr_{Ce}^{/} \tag{2.3}$$

where $Pr_{Ce}^{\times}$ and $Pr_{Ce}^{/}$ are Pr^{4+} and Pr^{3+}, respectively.

The corresponding mass action relation is

$$\frac{[Pr_{Ce}^{/}]}{[Pr_{Ce}^{\times}]n} = k_{Pr}^{\circ} \exp(-\frac{H_{Pr}}{kT}) = K_{Pr} \tag{2.4}$$

It is instructive to rewrite the reduction reaction, reaction (1), directly in terms of the Pr contribution to the reaction, particularly at high pO_2. Thus one can write:

$$2\,Pr_{Ce}^{\times} + O_O^{\times} \leftrightarrow 2\,Pr_{Ce}^{/} + V_O^{\bullet\bullet} + 1/2 O_2(g) \tag{2.5}$$

$$\frac{[Pr_{Ce}^{/}]^2[V_O^{\bullet\bullet}]pO_2^{1/2}}{[Pr_{Ce}^{\times}]^2[O_O^{\times}]} = k_{r,Pr}^{\circ} \exp(-\frac{H_{r,Pr}}{kT}) = K_{r,Pr} \tag{2.6}$$

It should be noted that Equation (2.6) is simply the product of Equation (2.1) and the square of Equation (2.4) and thus $H_{r,Pr} = H_r + 2H_{Pr}$. The effective reduction enthalpy, $H_{r,Pr}$, is thus reduced from that of undoped ceria, H_r, by twice the ionization energy of Pr, $2\,H_{Pr}$.

As the pO_2 is decreased, oxygen vacancies are generated through reaction 1 with the electrons thereby generated trapped on Pr sites via reaction (2.2) until all the Pr is reduced to the

trivalent state. At that point, PCO begins to behave like a conventional acceptor doped material, such as Gd or Sm doped ceria.

At sufficiently low pO_2, Ce cations themselves begin to reduce with oxygen vacancies generated, consistent with Equation 1 and the corresponding mass action relation given in Equation (2.2). The quasi-free electrons are now retained in the conduction band, made up of Ce 4f levels, and move between Ce ions via a small polaron hopping process. [80]

In order to maintain charge neutrality, the following equation applies

$$n + [\mathrm{Pr}'_{Ce}] = 2[\mathrm{V}_O^{\bullet\bullet}] \tag{2.7}$$

with the understanding that the concentrations of holes and oxygen interstitials are negligibly small under the present conditions. Mass and site conservation reactions are given by

$$[\mathrm{Pr}'_{Ce}] + [\mathrm{Pr}^{\times}_{Ce}] = [\mathrm{Pr}_{Ce}]_{\mathrm{total}} = 0.1[\mathrm{Pr}_{0.1}\mathrm{Ce}_{0.9}\mathrm{O}_{2-\delta}] \tag{2.8}$$

$$[\mathrm{V}_O^{\bullet\bullet}] + [\mathrm{O}^{\times}_O] = 2[\mathrm{Pr}_{0.1}\mathrm{Ce}_{0.9}\mathrm{O}_{2-\delta}] \tag{2.9}$$

where $[\mathrm{Pr}_{0.1}\mathrm{Ce}_{0.9}\mathrm{O}_{2-\delta}]$ is the concentration of PCO in #/cm^{-3}.

Additionally, the enthalpy of reduction of both undoped and Pr doped ceria have been reported to vary linearly with non-stoichiometry as: [79][81]

$$H_{r,\mathrm{Pr}} = H^{\circ}_{r,\mathrm{Pr}} + f\delta \tag{2.10}$$

with $\delta = [\mathrm{V}_O^{\bullet\bullet}]/[\mathrm{Pr}_{0.1}\mathrm{Ce}_{0.9}\mathrm{O}_{2-\delta}]$.

From Equation (2.1) to Equation (2.10), the pO_2 dependence of $[V_O^{\bullet\bullet}]$ and $[Pr_{Ce}^{/}]$ could be calculated, as shown in **Figure 1**.

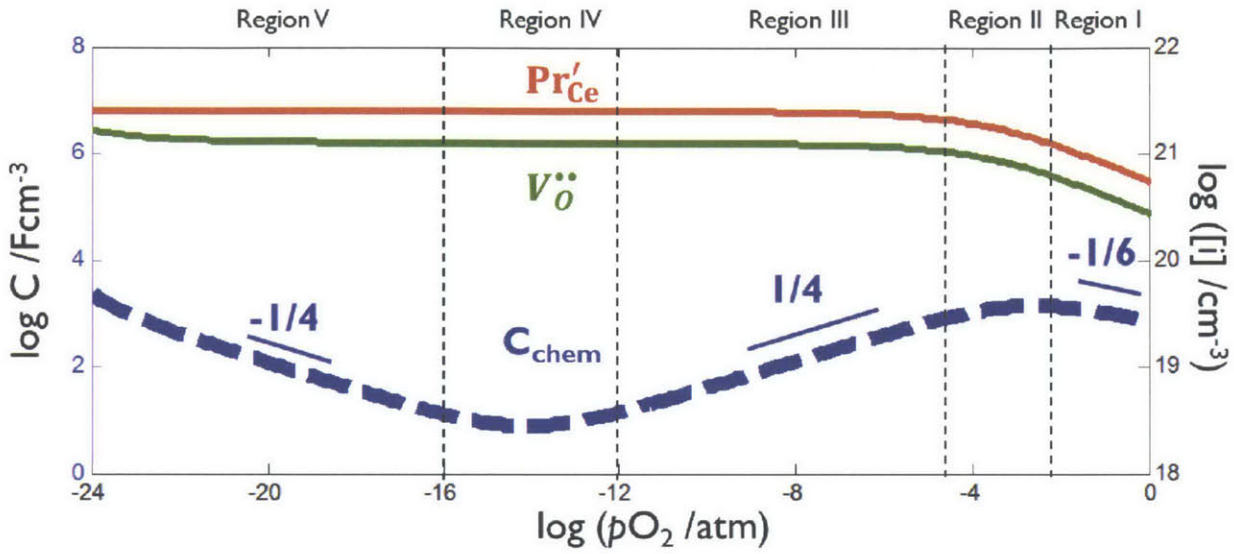

Figure 2.1 Predicted volume-specific C_{chem} (thick dash line) and defect concentrations (thin solid lines) derived from the PCO defect equilibrium model at 650°C.

2.2. Chemical Capacitance (C_{chem})

2.2.1. Relationship between δ and C_{chem}

The chemical capacitance (C_{chem}) is a measure of the chemical storage capacity of a material, in this case the formation/annihilation of oxygen vacancies and Pr^{3+}.[27][74][71] Capacitance is generally expressed as

$$C = \frac{dQ}{dE} \tag{2.11}$$

where Q is the charge stored for a given electrical potential, E.

Following the derivation of C_{chem} by Nakamura et al. [82], dQ is replaced by the amount of stored chemical species

$$dQ_{chem} = 2qV_{film}d[\mathrm{V}_O^{\bullet\bullet}] \tag{2.12}$$

where q and V_{film} are the elementary charge of an electron and volume of the film, respectively, with the factor of two representing the two charges per vacancy. Equation (2.12) is valid for uniform concentration of defects within a film, as in the case where surface oxygen exchange limits oxygen transport in and out of the film (as opposed to bulk diffusion limitation). dE is replaced by the Nernst potential for oxygen.

$$dE_{Nernst} = -\frac{kT}{4qpO_2}dpO_2 \tag{2.13}$$

where k and T are the Boltzmann constant and temperature, respectively, with ideal behavior of oxygen assumed.

Substituting Equations (2.12) and (2.13) into Equation (2.11) leads to the expression for C_{chem} as below.

$$C_{chem} = -\frac{8q^2V_{film}}{kT}\left(pO_2\frac{\partial[\mathrm{V}_O^{\bullet\bullet}]}{\partial pO_2}\right) \tag{2.14}$$

The film oxygen vacancy concentration can be estimated at each pO_2 through integration of Equation (2.14) with respect to pO_2 as

$$[\mathrm{V}_O^{\bullet\bullet}](pO_2) = \frac{kT}{8q^2V_{film}}\int C_{chem}\,d\ln pO_2 + [\mathrm{V}_O^{\bullet\bullet}](pO_2^{\circ}) \tag{2.15}$$

where pO_2° is a reference oxygen pressure at which $[\mathrm{V}_O^{\bullet\bullet}]$ is known.

2.2.2. C_{chem} of $Pr_{0.1}Ce_{0.9}O_{2-\delta}$

Figure 1 shows C_{chem} as a function of pO_2, calculated using Equation (2.14) and the pO_2 dependence of $[V_O^{\bullet\bullet}]$. In this figure, one observes an increase in vacancy and Pr^{3+} concentration with decreasing pO_2, corresponding to reduction and depletion of Pr^{4+}. Ultimately, at intermediate pO_2, $[V_O^{\bullet\bullet}]$ approximately saturates to half the total amount of Pr ($[Pr_{Ce}]_{total}$). At much lower pO_2 (not shown), Ce begins to reduce, resulting in a further increase of $[V_O^{\bullet\bullet}]$.

Interestingly, during this reduction process, the predicted C_{chem} exhibits five notable features: a power law dependence (slope = -1/6) in region I; a maximum, or peak, in region II; a power law dependence of opposite sign (slope = 1/4) in region III; a minimum in region IV; and a power law dependence (slope =-1/4) in region V. The peak in C_{chem} corresponds to the maximum change in $[V_O^{\bullet\bullet}]$ with pO_2 (approximately where Pr^{4+}/Pr^{3+} is unity), the minimum in C_{chem} corresponds to the minimum change in $[V_O^{\bullet\bullet}]$ with pO_2 (approximately where all Pr is Pr^{3+}), and the power law dependences arise from the pO_2 dependences of key defects within regions of pO_2 satisfying the Brouwer approximations of the defect equilibria. As shown in the discussion, all five features exist in the *measured* C_{chem}, serving as an excellent demonstration of the self consistency between these measurements and the predicted defect equilibria.

2.3. Simplification of C_{chem} in $Pr_{0.1}Ce_{0.9}O_{2-\delta}$

A key objective of this study is to demonstrate the ability to extract oxygen non-stoichiometry of a thin film using chemical capacitance. In order to obtain absolute values for δ at any given temperature and pO_2, using Equation (2.15), the absolute value of non-stoichiometry, $[V_O^{\bullet\bullet}](pO_2^{\circ})$, must be known at some reference oxygen partial pressure pO_2°. Fortunately, reliable

reference values for $[V_O^{\bullet\bullet}]$ can be obtained directly from measurements of C_{chem}, based on the simplification of the defect chemical model in different regions, as described in the following.

2.3.1. Simplification at high pO_2

Considering defect region I, in Figure 1, nearly all of the Pr ions are oxidized to Pr^{4+}, thus

$$[Pr_{Ce}^{\times}] \approx [Pr_{Ce}]_{\text{total}} \tag{2.16}$$

The condition for charge neutrality is given by

$$[Pr_{Ce}^{/}] = 2[V_O^{\bullet\bullet}] \tag{2.17}$$

Substitututing Equations (2.16) and (2.17) into Equation (2.6), and solving for $[V_O^{\bullet\bullet}]$ leads to

$$[V_O^{\bullet\bullet}] = (\frac{1}{4} K_{r,\mathrm{Pr}} [Pr_{Ce}]_{\text{total}}^2 [O_O^{\times}])^{1/3} pO_2^{-1/6} \tag{2.18}$$

Substituting this into the definition of chemical capacitance, Equation (2.14), one obtains an expression showing the predicted pO_2 dependence of C_{chem}.

$$C_{chem} = \frac{4}{3} \frac{q^2 V_{film}}{kT} (\frac{1}{4} K_{r,\mathrm{Pr}} [Pr_{Ce}]_{\text{total}}^2 [O_O^{\times}])^{1/3} pO_2^{-1/6} \tag{2.19}$$

Noting the definition for $[V_O^{\bullet\bullet}]$ in Equation (2.18), and substituting this back into Equation (2.19) leads to

$$C_{chem} = \frac{4}{3} \frac{q^2 V_{film}}{kT} [V_O^{\bullet\bullet}] \tag{2.20}$$

In contrast to prior investigations of C_{chem} in oxide films (where fitting parameters are used), this approach allows a direct determination of $[V_O^{\bullet\bullet}]$ at any pO_2 from a measurement of C_{chem} with only knowledge of film volume and total Pr concentration, as long as the approximation in Equation (2.16) is valid. Such experimentally derived values can then be used to establish reference values for $[V_O^{\bullet\bullet}](pO_2^{\circ})$ in Equation (2.15) and thereby solve for values of $[V_O^{\bullet\bullet}](pO_2)$ not falling within the defect regimes satisfying the Brouwer approximations.

Turning to lower pO_2 (region III), where nearly all the Pr is reduced to Pr^{3+}, the charge neutrality equation (Equation (2.7)) can be approximated by:

$$[Pr_{Ce}'] = 2[V_O^{\bullet\bullet}] \approx [Pr_{Ce}]_{total} \tag{2.21}$$

Though in this region, Pr exists largely as Pr^{3+}, a small concentration of Pr^{4+} remains, with its concentration derived by substituting Equation (2.17) into Equation (2.8), yielding:

$$[Pr_{Ce}^{\times}] \approx [Pr_{Ce}]_{total} - 2[V_O^{\bullet\bullet}] \tag{2.22}$$

Substituting $[Pr_{Ce}]_{tot}$ for $[V_O^{\bullet\bullet}]$ and $[Pr_{Ce}']$ using Equation (2.21) and the r.h.s. of Equation (2.22) for $[Pr_{Ce}^{\times}]$ into Equation (2.6), and solving for $[V_O^{\bullet\bullet}]$ leads to:

$$[V_O^{\bullet\bullet}] = \frac{[Pr_{Ce}]_{total}}{2} - \frac{1}{2}\left(\frac{1/2[Pr_{Ce}]_{total}^3 pO_2^{1/2}}{K_{r,Pr}[O_O^{\times}]}\right)^{1/2} \tag{2.23}$$

Substituting this result into the definition of chemical capacitance, Equation (2.14), one obtains an expression showing the predicted pO_2 dependence of C_{chem}

$$C_{chem} = \frac{q^2 V}{kT}\left(\frac{1/2[\mathrm{Pr}_{Ce}]^3_{\mathrm{total}}}{K_{r,\mathrm{Pr}}[\mathrm{O}_O^{\times}]}\right)^{1/2} pO_2^{1/4} \tag{2.24}$$

Noting the definition for $[\mathrm{V}_O^{\bullet\bullet}]$ in Equation (2.23), and substituting this back into Equation (2.24) leads to

$$C_{chem} = \frac{q^2 V}{kT}([\mathrm{Pr}_{Ce}]_{\mathrm{total}} - 2[\mathrm{V}_O^{\bullet\bullet}]) \tag{2.25}$$

One last point worth mentioning here, is that in the above derivation, the dependence of $H_{\mathrm{r,Pr}}$ on δ was assumed negligible, a valid approximation considering the relatively small changes in $[\mathrm{V}_O^{\bullet\bullet}]$ in regions I and III.

2.3.2. Simplification at low pO_2

At low pO_2 (region V in Figure 1), $n << 2[\mathrm{Pr}'_{Ce}]$ so that $[\mathrm{Pr}'_{Ce}] \approx 2[\mathrm{V}_O^{\bullet\bullet}] \approx$ constant which, when introduced into Equation (2.2), results in the following expression.

$$n \approx \sqrt{\frac{2K_r[O_O^{\times}]}{[\mathrm{Pr}'_{Ce}]}}\, pO_2^{-1/4} \tag{2.26}$$

Substituting Equation (2.26) into Equation (2.7) results in the following equation for oxygen vacancy concentration:

$$[\mathrm{V}_O^{\bullet\bullet}] \approx \frac{1}{2}[\mathrm{Pr}'_{Ce}] + \sqrt{\frac{2K_r[O_O^{\times}]}{[\mathrm{Pr}'_{Ce}]}}\, pO_2^{-1/4} \tag{2.27}$$

Substituting the derivative of Equation (2.27) with respect to pO_2 into Equation (2.14) leads to

$$C_{chem} \approx \frac{q^2 V_{film}}{kT} \sqrt{\frac{2K_r[O_O^{\times}]}{[Pr_{Ce}^{/}]}} pO_2^{-1/4} \tag{2.28}$$

Comparing Equation (2.27) and (2.28), it becomes obvious that Equation (2.27) can be rewritten in terms of C_{chem} as:

$$[V_O^{\bullet\bullet}] \approx \frac{1}{2} \frac{k_B T}{q^2 V_{film}} C_{chem} + \frac{1}{2}[Pr_{Ce}^{/}] \tag{2.29}$$

This approach allows a direct measure of $[V_O^{\bullet\bullet}]$ at any pO_2 from a measurement of C_{chem} with only knowledge of film volume and total Pr concentration as long as the approximation $[Pr_{Ce}^{/}] \approx 2[V_O^{\bullet\bullet}] \approx$constant remains valid.

2.4. The effective pO_2 caused by bias

In an MIEC electrode such as PCO, three key rate limiting processes need to be considered for oxygen transport from the gas phase into the dense electrode and ultimately into the electrolyte. These are (i) oxygen surface exchange at the electrode-gas interface, (ii) mass transport through the electrode, and (iii) transfer of oxygen ions across the PCO/ YSZ interface, as shown in **Figure 2.2** (a). If the surface reaction is the limiting step, when a small DC bias ΔE is applied on the electrode, the effective oxygen potential on the electrode surface would be $ze\Delta E$. The oxygen potential profile in the film is shown in Figure 2.2 (b).[27][39] The oxygen potential in the electrode is

$$\mu_{O_2,eff} = \mu_{O_2,g} + ze\Delta E \tag{2.30}$$

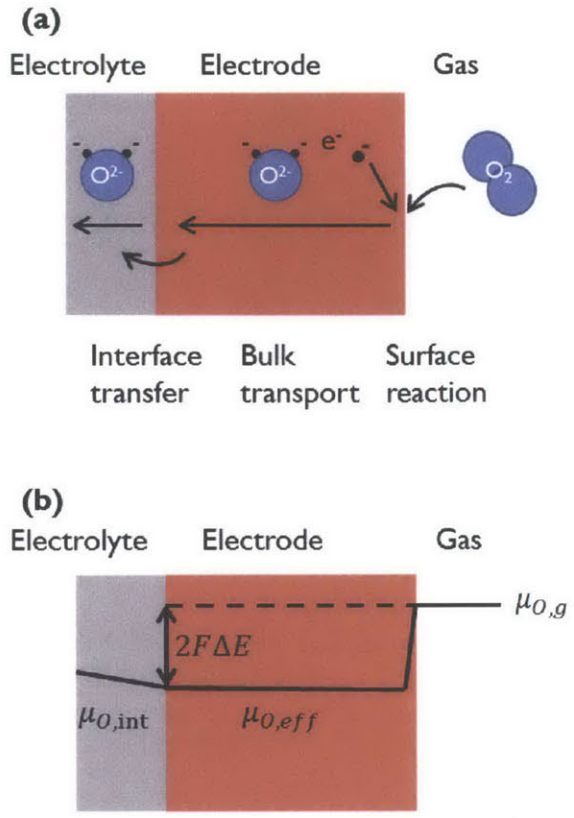

Figure 2.2 (a) Typical dominant reaction paths for oxygen reduction on MIEC electrode. (b) Corresponding oxygen potential profile around a dense conductor electrode when a small voltage perturbation ΔE is applied to the electrode (e.g., in impedance measurement). For clarity, bulk transport and interface transfer are assumed to be fast, so there is no potential drop in electrode and electrode/electrolyte interface.

The effective oxygen partial pressure in the electrode can be written as

$$pO_{2,eff} = pO_{2,g} \exp(\frac{ze\Delta E}{kT}) \tag{2.31}$$

3. CHAPTER 3 EXPERIMENTAL

3.1. Sample preparation

3.1.1. PLD target preparation

$Pr_xCe_{1-x}O_{2-\delta}$ targets with x = 0.01, 0.1, 0.2 (denoted throughout the text as PCO100x; i.e. PCO10 is for x = 0.1) were fabricated from PCO powders prepared through a Pechini-based gel process described briefly below [83]. The following starting materials were utilized: cerium (III) nitrate hexahydrate, 99.99% (Sigma Aldrich), praseodymium (III) nitrate hydrate, 99.9%, ethylene glycol (Alfa Aesar) and anhydrous citric acid (Fisher Scientific). Citric acid and ethylene glycol were mixed with aqueous solutions of $Ce(NO_3)_3$ and $Pr(NO_3)_3$ at 80 °C until polyesterification resulted in the formation of a gel. After drying in an oven at 110 °C, the as-obtained powder was fired at 450 °C for 4 hours and then at 700 °C for 3 hours in flowing air. The PCO powders were examined by X-ray diffraction (Rigaku H3R Cu-source Powder Diffractometer) and were found to have a single phase fluorite structure. Approximately 20 g of powder was loaded into a cylindrical stainless steel die of 1 inch diameter and uniaxially-pressed at 23 MPa for 90 seconds. The target was then placed in a plastic bag, evacuated, and pressed in a cold isostatic press at 275 MPa for two minutes. After pressing, the target was sintered at 1450°C for 6 hours in N_2 to approximately 93% theoretical density.

3.1.2. PLD film deposition

PCO films were prepared by PLD from oxide targets. The films were deposited onto (001) oriented single crystal YSZ (8 mol% Y_2O_3 stabilized) substrates (10 × 10 × 0.5 mm^3; MTI Corporation, Richmond, CA). The PLD system (Neocera Inc., Beltsville, ML) was operated with a KrF excimer laser (Coherent COMPex Pro 205), emitting at 248 nm, at energy of 400 mJ/pulse

and with a repetition rate of 8 Hz. The substrates were heated to 725 °C during deposition, while the oxygen pressure was maintained at 10 mTorr after pumping the background pressure to less than 9×10^{-6} Torr. Following deposition and prior to cooling, the oxygen pressure in the chamber was increased to approximately 6-7 Torr to facilitate more complete oxidation of the films. Figure 1 is a photograph of a PCO film prepared by PLD. Its reddish color is a consequence of a photon induced transition of electrons from the ceria valence band to Pr^{4+} levels lying within the ceria band gap [5].

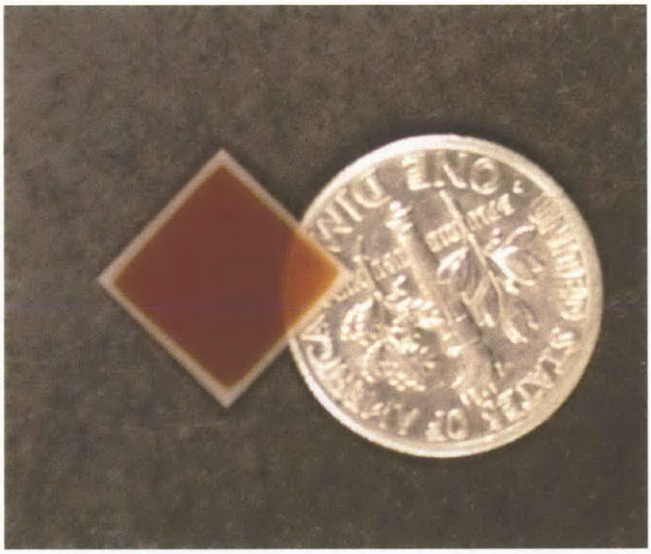

Figure 3.1 Photograph of a PCO10 film deposited onto a YSZ substrate by PLD.

3.2. Physical Characterization

3.2.1. Atomic Force Microscopy and Profilometer

The approximate grain size and surface roughness of the PCO thin films were measured by atomic force microscopy (Digital Instruments Nanoscope IIIa). The microscope was operated in tapping mode using a standard Si-based cantilever (Veeco Probes, model RTESP). The tip length and radius were 125 μm and approximately 10 nm, respectively. Samples were measured in air

with no additional preparation. The target amplitude was set to 2 V and an automatic algorithm was used to tune and detect the resonance frequency of each tip. The z-axis limit of the microscope was reduced from 8 to 1 μm in order to improve the resolution of the surface micrographs. Micrographs were analyzed to determine the root mean square (RMS) surface roughness and grain size using Vecco's Nanoscope software (version 5.12r3).

Film thickness, ranging between 100 and 600 nm, was determined by taking the height difference with a surface profilometer (KLA-Tencor P-16+ stylus profiler) between masked and unmasked areas.

3.2.2. X-ray Diffraction

X-ray Diffraction (XRD; X'Pert PRO MPD, PANalytical) was performed on the PCO films. The objective of the XRD measurements was to obtain information on the degree of crystallization, on the nature of the crystal phases, and the preferential orientation. Programmable Divergence Slit (PDS) was used on the incident-beam side. 2 mm Incident-Beam Anti-Scatter Slit was used to match the PDS. The Soller slit used was 0.04 rad while the Beam mask was 10 mm. Diffraction patterns were analyzed using the software package High Score Plus, from PANalytical and compared against standards from the ICCD powder diffraction file.

3.3. EIS measurement

3.3.1. Cell preparation

Two different sample geometries were prepared for EIS measurements: a symmetrical structure with identically sized (9×9 mm^2) PCO electrodes on both sides of the YSZ electrolyte, and an asymmetrical structure of 1 – 10 mm diameter PCO working electrodes with a porous Ag counter electrode (SPI Silver Paste Plus, SPI Supplies, Chester, PA, USA) on the opposite side

of the YSZ substrate/electrolyte. In both configurations, Au paste (Fuel cell materials, Lewis Center, Ohio), serving as a current collector, was applied to the top surface of the PCO electrode. For bias controlled measurements, a reference electrode was added on edge of the electrolyte of the asymmetrical cell, to enable the application of a DC bias between it and the working electrode (see Fig. 2c).

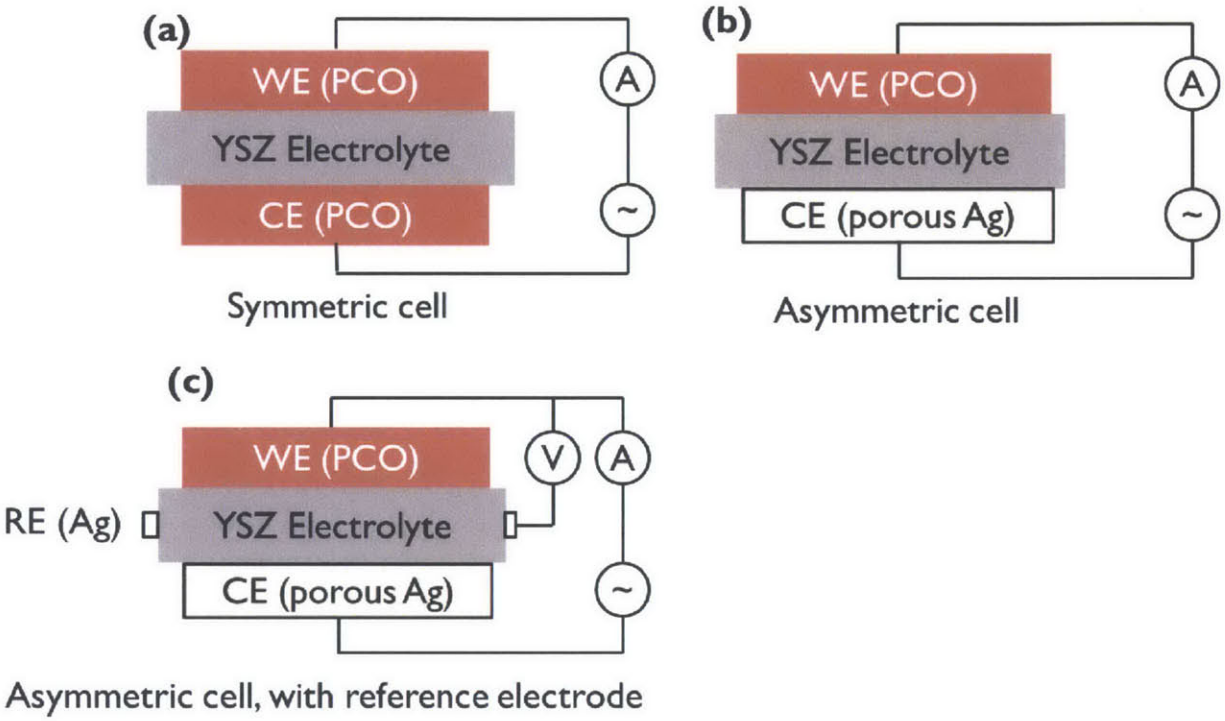

Figure 3.2 Schematic illustrations of different cell geometries: (a) a symmetrical structure with identically sized PCO electrodes on both sides of the YSZ electrolyte, (b) an asymmetrical structure in which a porous Ag counter electrode was applied to one side of the YSZ, and (c) an asymmetrical structure in which a Ag reference electrode was applied on the side of the YSZ electrolyte.

3.3.2. Measurement conditions

Electrochemical impedance spectroscopy (EIS) measurements, covering the frequency range from 1 MHz to 0.032 Hz, were performed using an impedance analyzer (Solartron 1260) with the data fit with equivalent circuits using Zview and Zplot software (Scribner Associates). AC

amplitudes of 10 and 20 mV were used throughout, after tests had shown that these voltages lies within the linear regime of the sample's current-voltage response. In additions, a DC bias range of ΔE = -100 mV to 100 mV was used to enable polarization of the electrodes and examine the impact on ASR and film stoichiometry.

The EIS measurements were performed at temperatures between 450 and 800 °C and oxygen partial pressures between 10^{-33} and 1 atm in a tube furnace (Lindberg). Mass flow controllers (MKS) connected to O_2, N_2, CO, CO_2, H_2 and H_2O were controlled with a custom-designed mass flow programmer. The pO_2 was monitored by an in-situ YSZ Nernst type oxygen sensor. Samples were electrically contacted with 250 µm diameter, 99.99% pure platinum wire (Alfa Aesar). The wires are mounted to the current collector and conter electrode using silver paste (SPI Silver Paste Plus, SPI Supplies, Chester, PA, USA).

3.4. Data fitting

Data fitting to defect models to obtain thermodynamic parameters was performed using Matlab (Mathworks). Parameters in the models were determined using the Gauss-Newton method of non-linear regression, with partial derivatives approximated numerically [84]. Initial estimations were refined visually and then regression was performed in a step-wise iterative manner. Error estimates for modeled parameters are reported for an approximate 95% confidence interval of the regressed model.

4. CHAPTER 4 RESULTS

4.1. Physical Characterization of PCO films

Figure 4.1 shows the XRD pattern obtained from 2θ-ω coupled scans of the YSZ single crystal with (Figure1.a) and without the 10PCO film (Figure1.b). Only the {001} peaks are observed for the film, which confirms that the PLD films exhibited the fluorite structure with highly (100)-orientated texture.

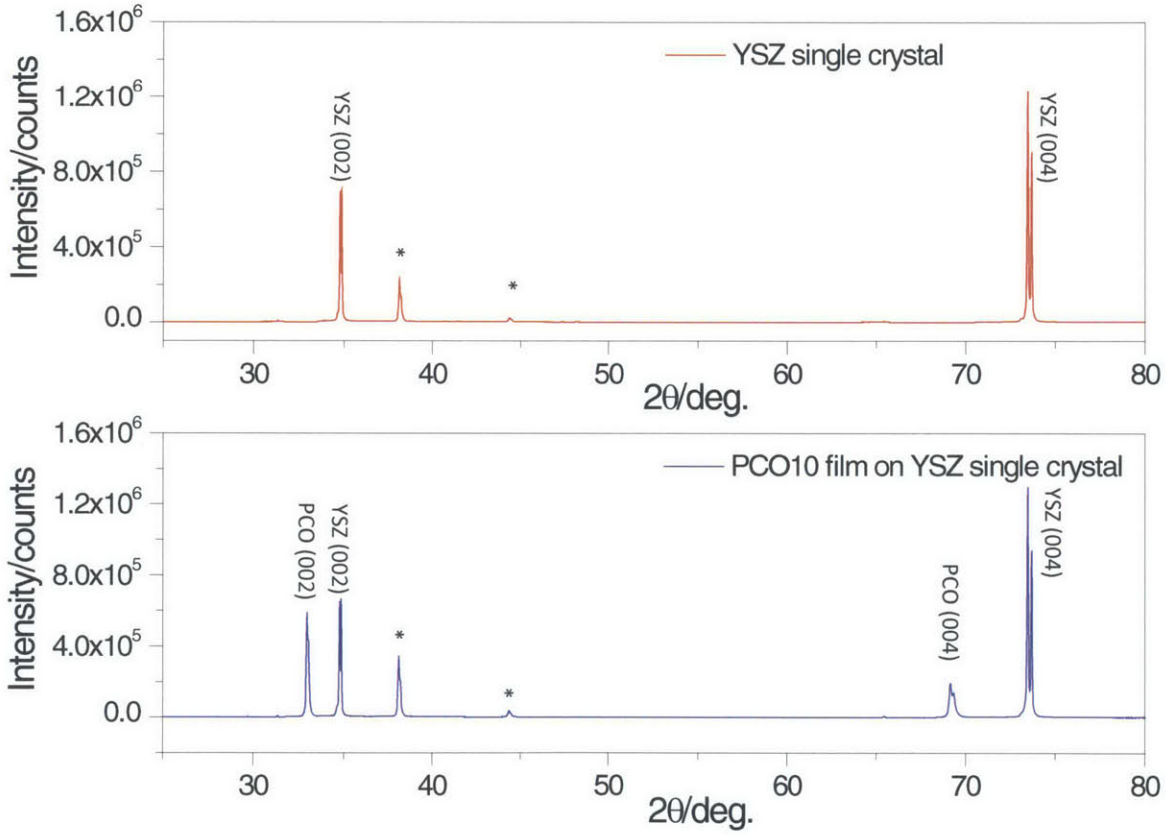

Figure 4.1 XRD analysis of the as-deposited PCO10 film on YSZ (001) substrate (a) XRD 2θ-ω coupled scan on YSZ single substrate; (b) XRD 2θ-ω coupled scan on PCO10 film deposited on YSZ single substrate. The asterisks denote peaks from secondary radiation (i.e. non-Cu-k_α radiation).

Atomic force microscope (AFM) image of the surface of as-deposited PCO10 film is shown in **Figure 4.2**. A root-mean-square (RMS) surface roughness was calculated after

averaging three different measurements on the same film. The AFM results showed a dense and smooth film indicating a grain size of approximately 50 nm and surface roughness of approximately 0.5 nm.

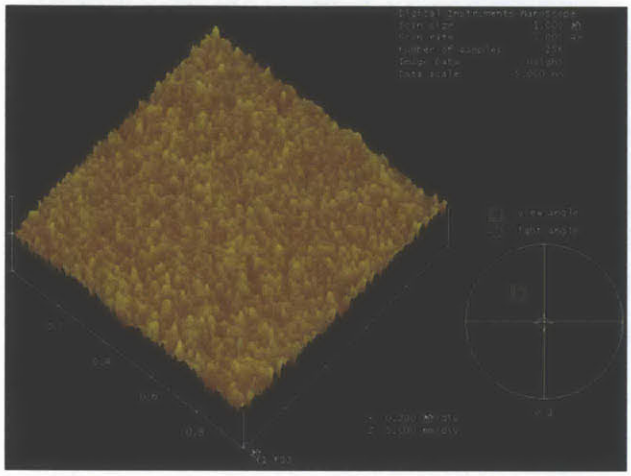

Figure 4.2 AFM micrograph of PCO10 surface deposited on YSZ single crystal.

4.2. EIS of PCO electrode

Figure 4.3 shows typical impedance results obtained for the asymmetric cell PCO10/YSZ/Ag. The spectrum exhibits two adjacent semicircles offset from the origin. The one at higher frequencies is smaller and more highly distorted. The second, at lower frequency, is larger and is a near-ideal semicircle.

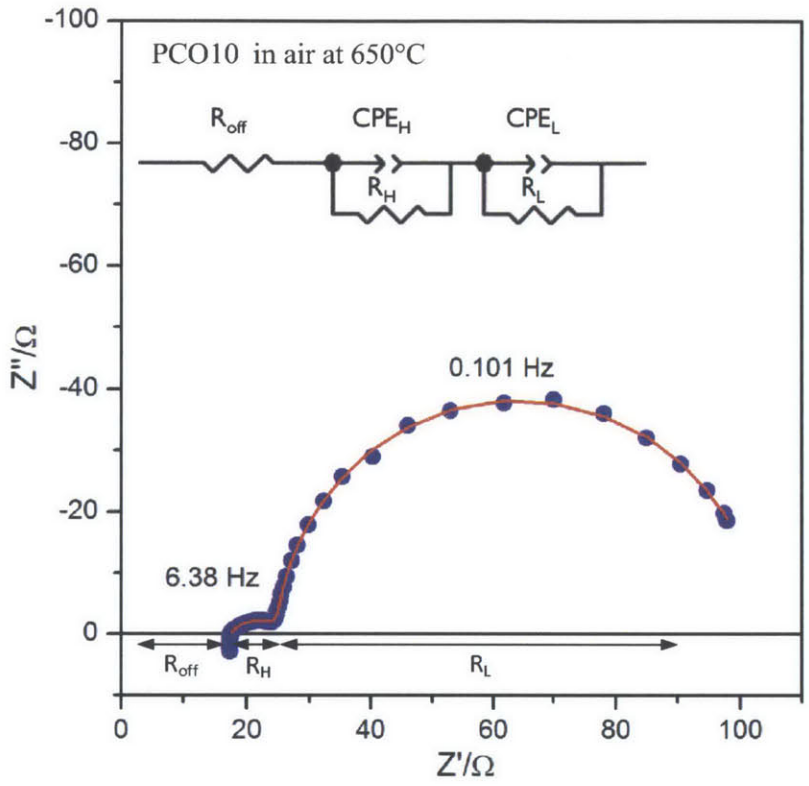

Figure 4.3 Typical impedance spectra of an asymmetric cell of PCO10/YSZ/Ag at 650°C in air, where variables are defined in the text. Film thickness is 249 nm and the denoted frequencies correspond to the top, or peak magnitude of Z" in their respective semi-circles. Inset shows the equivalent circuit fit to the data using the Zview program.

One can assign this response to a resistor in series with two *R-Q* circuits (*R-Q*: a resistor in parallel with a constant phase element [CPE]) as shown by the inset in Figure 4.3. The three resistors are defined as R_{off}, R_H and R_L and their origins are defined later. CPEs are used given that electrode impedances are typically characterized by a distribution of time constants resulting from morphological variations within the electrode and at the electrode/electrolyte interfaces resulting in "depressed" arcs not well represented by an ideal capacitor [85]. The impedance of a constant phase element is given by

$$Z = \frac{1}{Q(i\omega)^n} \tag{4.1}$$

from which the capacitance is derived using the following equation [86]

$$C = Q\omega_{\max}^{n-1} = \left(R^{1-n}Q\right)^{1/n} \tag{4.2}$$

The fit, applying the equivalent circuit (shown in the inset of Figure 4.3) to the data, is observed to be quite good. The second semicircle has a typical n value between 0.979 and 0.997.

4.3. Geometry dependence of impedance spectra

4.3.1. Symmetric vs. asymmetric cell

Figure 4.4 shows impedance results obtained for both the symmetric and asymmetric structures with the PCO10 film electrodes. Going from the asymmetric to the symmetric cell, the high frequency semicircle disappears while the diameter of the low frequency semicircle doubles in magnitude. Given that the only features in the impedance spectrum of the symmetric structure is the semicircle with diameter of 155 Ω and the previously defined R_{off}, the semicircle can confidently be assigned to the PCO electrodes, with each electrode contributing half this value (~77 Ω). On the other hand, the asymmetric structure exhibits both a small distorted high frequency semicircle with a 9.5 Ω diameter and a nearly ideal low frequency semicircle with a 79.9 Ω diameter. Comparing the two structures, it becomes obvious that in the asymmetric structure, the larger low frequency semicircle (roughly half that in the symmetric structure, characterized by R_L and C_L) should be assigned to the PCO electrode, while the smaller high frequency semicircle (characterized by R_H and C_H) should be attributed to the porous Ag electrode.

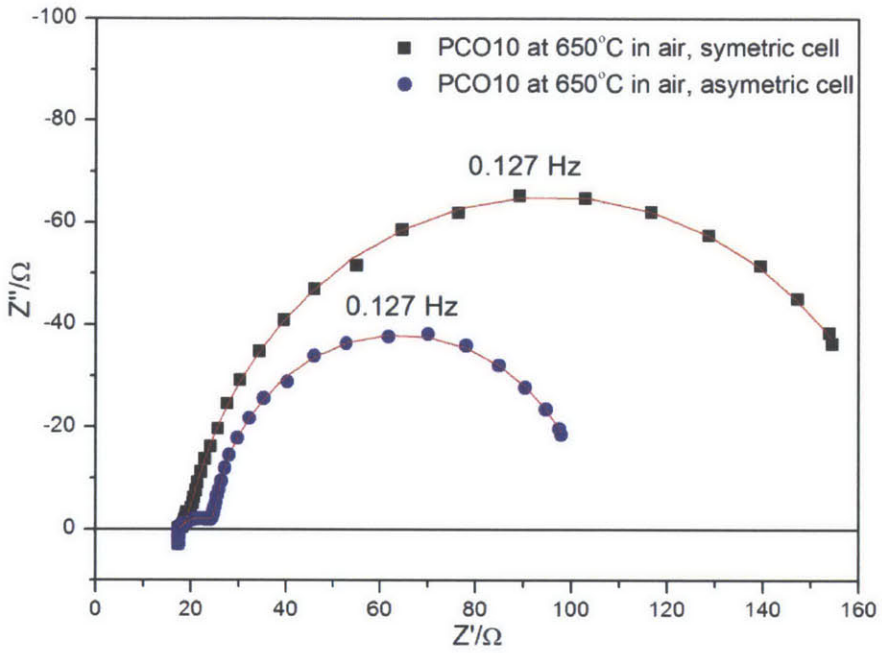

Figure 4.4 Complex Impedance plot of symmetric and asymmetric cell of PCO10 at 650 °C in air with peak frequencies indicated.

4.3.2. Area dependence of impedance spectra

Given the ability to confirm that the low frequency semicircle comes from the PCO electrode, the R and C values derived from this part of the impedance spectra are therefore designated as R_{PCO} and C_{PCO}. In the following, the focus shifts to identifying the electrode processes controlling R_{PCO} and C_{PCO}. To identify the electrode process controlling R_{PCO} and C_{PCO}, their surface area and thickness dependence is studied. Log *R*PCO and Log C_{PCO} for PCO10 is plotted vs. log (electrode area, S) in **Figure 4.5** and shows a power law dependence of -1 and 1.

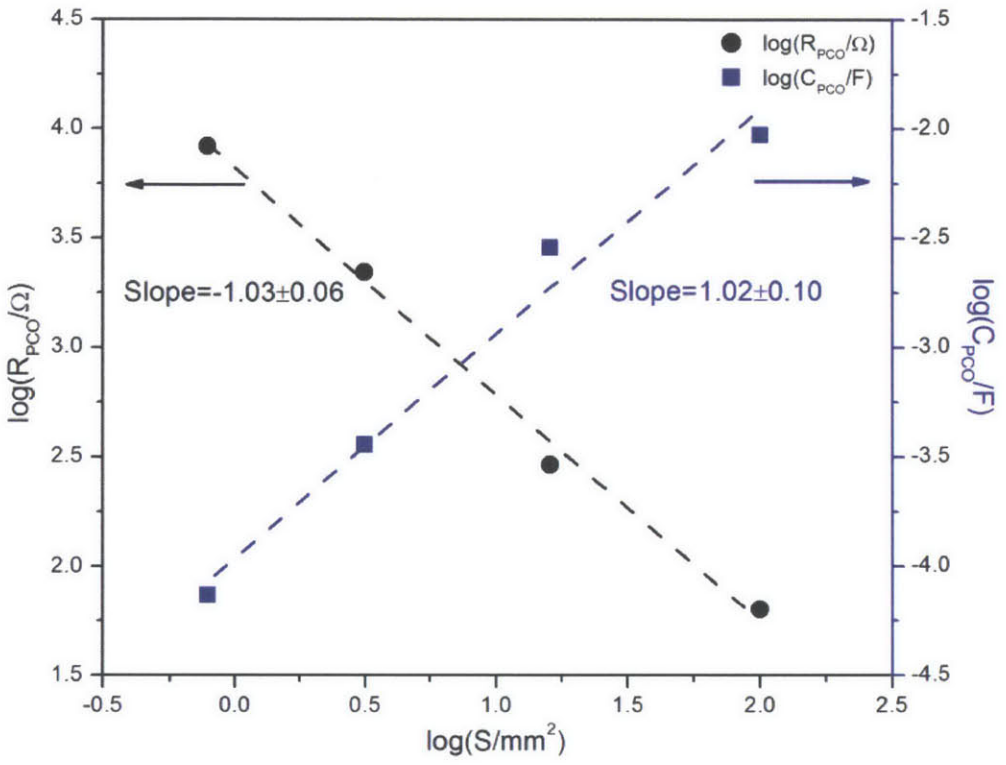

Figure 4.5 Double-logarithmic plots of R_{PCO} and C_{PCO} for the PCO10 electrode vs surface area (S), measured at 670 °C in air using the asymmetric cell configuration.

4.3.3. Thickness dependence of impedance spectra

In **Figure 4.6**, log *R*PCO vs T^{-1} is plotted with film thicknesses, h varying by as much as a factor of 3. R_{PCO} is observed, within experimental error, to be independent of film thickness. R_{PCO} for PCO1 and PCO20 films showed a similar geometrical dependence. In **Figure 4.7**, *CPCO* for PCO10 is plotted vs. thickness, and shows a power law dependence of 1 at different temperatures.

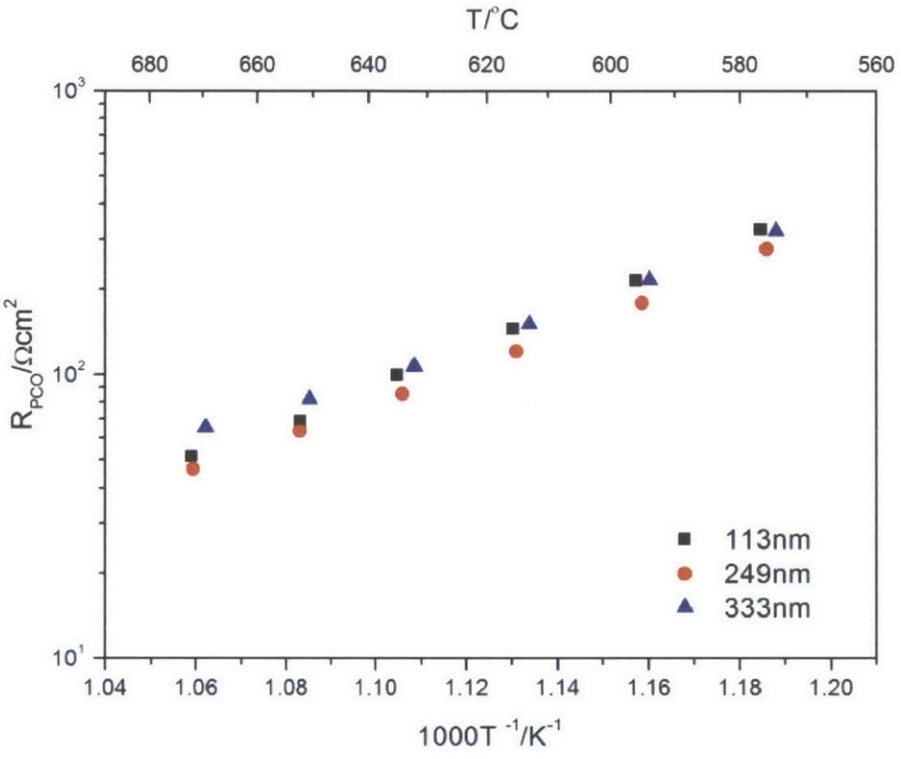

Figure 4.6 Temperature dependence of R_{PCO} for PCO10 electrodes with three different film thicknesses, as indicated. Measured in air using the asymmetric cell configuration.

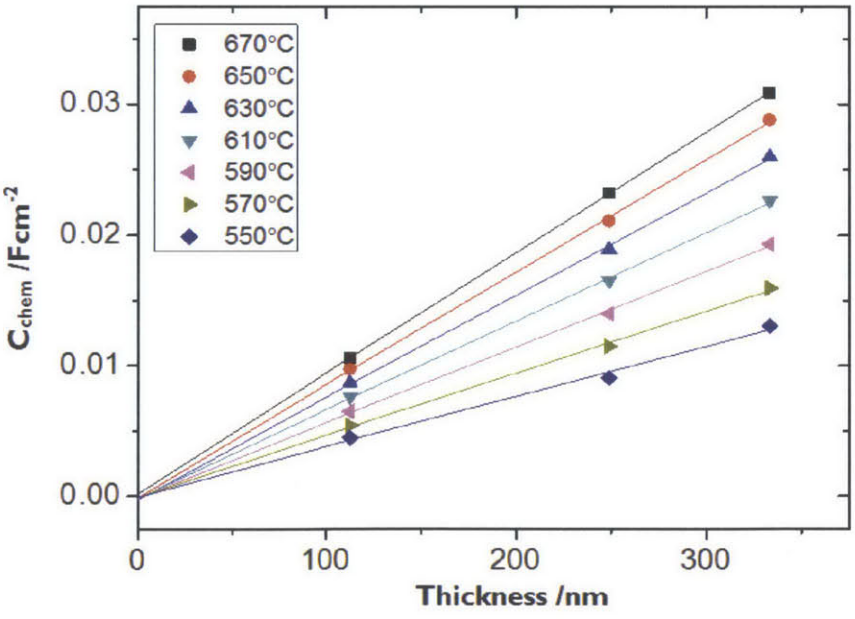

Figure 4.7 Thickness dependence of C_{PCO} of a PCO10 electrode measured at different temperatures in air using the asymmetric cell configuration.

4.4. Temperature and pO_2 dependence of impedance spectra

4.4.1. Temperature and pO_2 dependence of impedance spectra

Under all experimental conditions, the measured impedance spectra of the symmetric cell PCO/YSZ/PCO were nearly perfect semicircles, displaced from the origin on the real axis, as shown in **Figure 4.8** with data collected at 700 °C as a function of pO_2. As shown in the inset, the spectra are represented by a resistor in series with a R//C circuit. The equivalent circuit fits are observed to represent the data well.

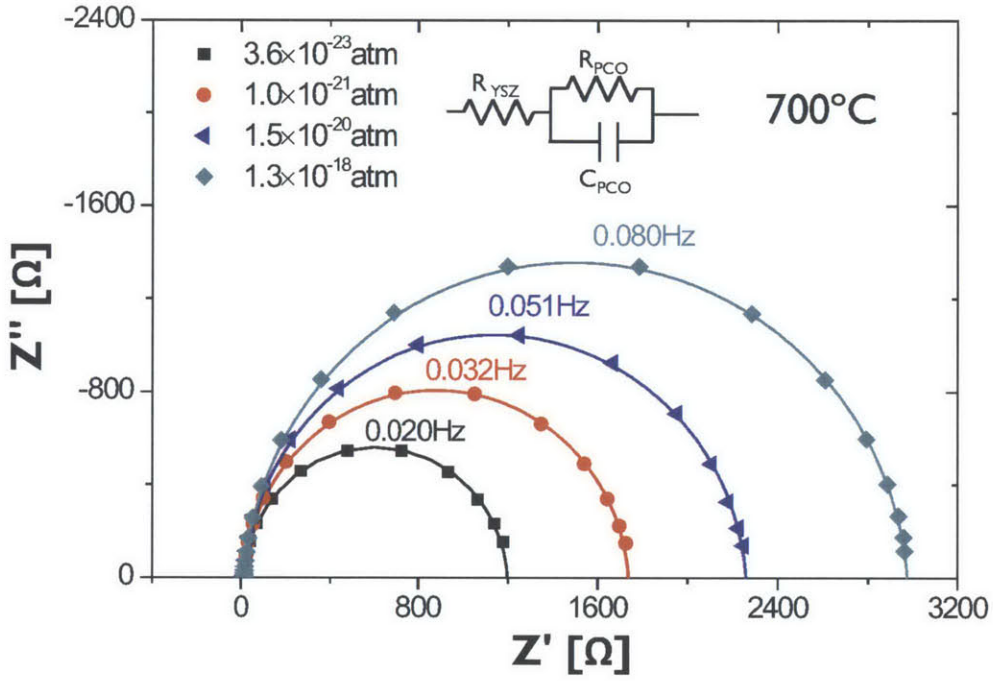

Figure 4.8 Typical impedance spectra of a symmetric cell of PCO/YSZ/PCO with PCO film thickness of 131 nm at 700 °C at various oxygen partial pressures as indicated. The symbols are the experimental data while the solid lines are the equivalent circuit fit. The inset shows the equivalent circuit used to fit the data. Frequencies near the semi-circle peak are indicated.

4.4.2. Temperature and pO_2 dependence of R_{off}

In **Figure 4.9(a)**, R_{off}, extracted from the impedance spectra obtained for the asymmetric cell, and normalized to the geometry of the cell, is plotted as log $\square T$ vs T^{-1} to facilitate calculation of an activation energy (E_A), consistent with the following equation.

$$\sigma = \frac{\sigma_\circ}{T}\exp\left(-\frac{E_A}{kT}\right) \tag{4.3}$$

The data obtained in this study are characterized by E_A = 1.14 ± 0.03 eV, typical of values obtained for ionic conduction in YSZ [87]. In **Figure 4.9(b)**, the offset resistance is recalculated as above and plotted as log $\square$ vs log $pO2$, and within experimental error, one finds that this resistance is independent of pO_2. R_{off} derived from the impedance spectra of cells using PCO1 and PCO20 exhibit a similar temperature and $pO2$ dependence.

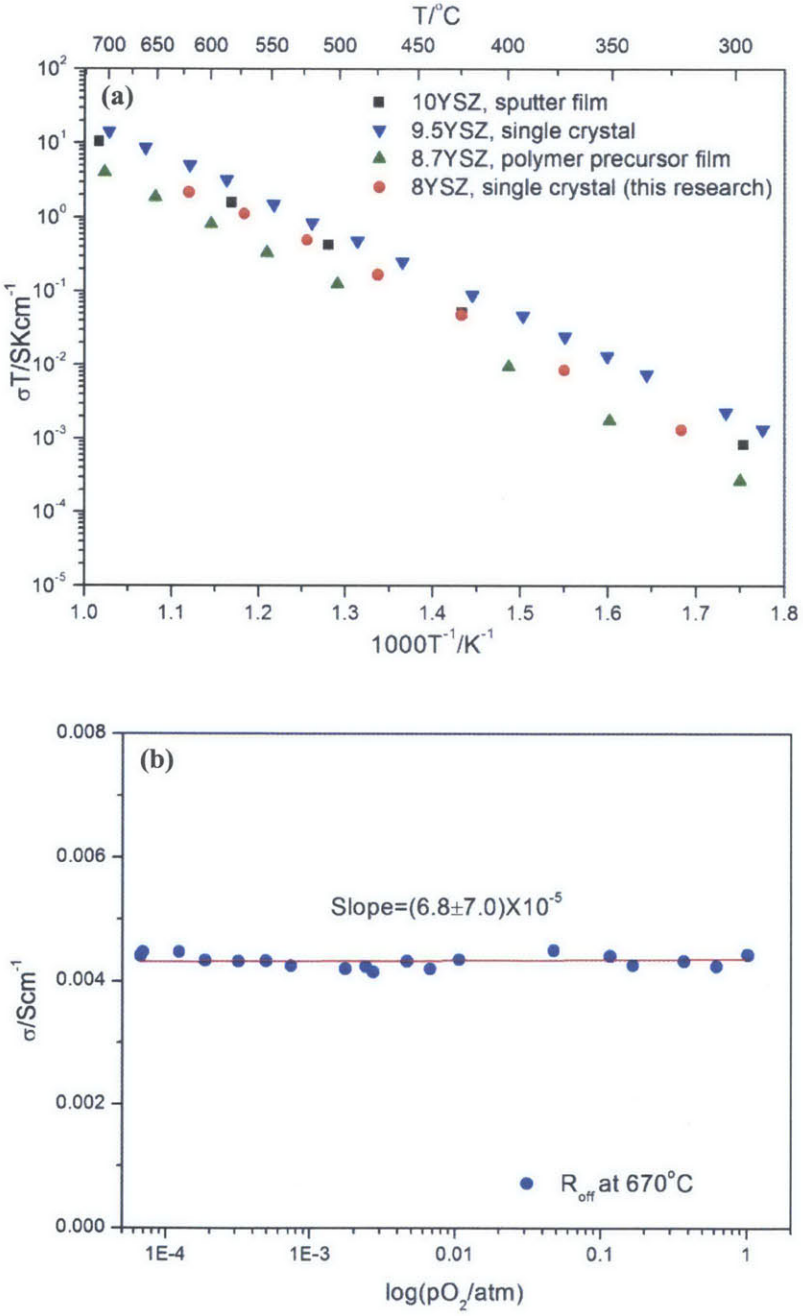

Figure 4.9 (a) Temperature dependence of σT extracted from R_{off} using the substrate dimensions in the conductivity calculation for a PCO10 sample in air and, compared with:

10 mol% YSZ film [88] , 9.5 mol% YSZ single crystal [89], and 8.7 mol% YSZ film [90] (b) Oxygen partial pressure dependence of σ calculated from R_{off} measured at 670 °C.

4.4.3. Temperature and pO_2 dependence of C_{PCO}

The experimentally derived values for C_{chem} of the symmetric cell are plotted as a function of pO_2 for a series of isotherms in **Figure 4.10** and **Figure 4.11 (a)** for high pO_2 and low pO_2 region, respectively. In Figure 4.9, the solid curves represent the calculated values of C_{chem}, derived with the aid of Equation (2.15) and using $[V_O^{\bullet\bullet}]$ values extracted from the defect model (fitted to the C_{chem} data as discussed later). The first point to note is the replication of features discussed in Figure 4.9, particularly the clear peak in C_{chem}, visible for data above 550 °C and the power law dependences. Good agreement between predicted and measured data is observed, though above 700 °C, only the shapes of the curves remain in good agreement, with an approximate 60% deviation of the model from the data. In this high temperature region, the PCO impedance spectra deviated from the ideal case in Figure 4.3. The possible reasons will be discussed in Chapter 5.

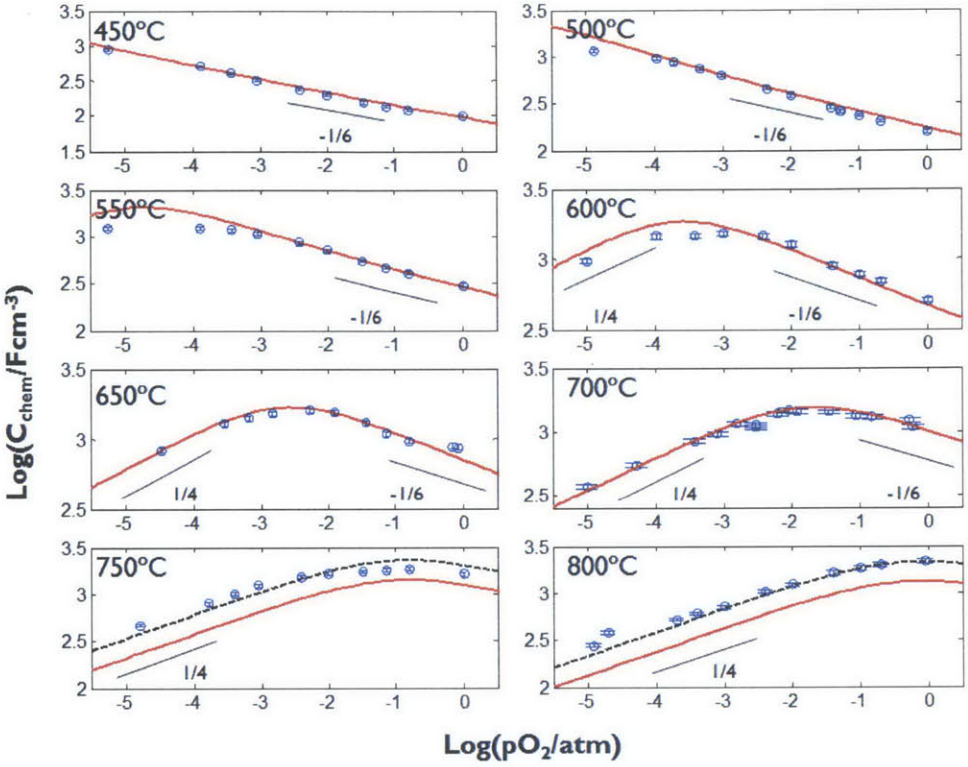

Figure 4.10 Isothermal dependence of volume-specific C_{chem} (circles) on pO_2, obtained from a symmetric PCO/YSZ/PCO cell with PCO film thickness of 113 nm. Solid lines represent modeled data and dashed lines, for 750 °C and 800 °C, are 1.6 times the modeled data.

In Figure 4.11(a), three trends are apparent for these low pO_2 data: 1) the capacitance increases with increasing temperature, 2) the capacitance shows a -1/4 slope on the log-log plot at low pO_2 consistent with Equation (2.28), and 3) at higher pO_2 the capacitance values tend to saturate to a common value of log C_{PCO} ~ -3.6. Chueh and Haile previously demonstrated a strong deviation of log C from the expected -1/4 slope for Sm doped ceria under similar conditions to those in our study, and attributed this to the presence of a second, constant capacitance term [77]. This additional contribution is incorporated using the following equation

$$C_{\text{total}} = C_{chem} + C_{\text{constant}} \tag{4.4}$$

The values of C_{chem} are plotted as a function of pO_2 in Figure 4.11(b) following the subtraction of $C_{constant}$ derived in Figure 4.11(a) from the measured values of C_{total}. In our measurements at high pO_2, the C_{PCO} values were more than two orders of magnitudes larger than those measured here, (e.g. the smallest value of C_{PCO} measured was 0.04 Fcm^{-2}). No saturation in C_{total} was detected under those circumstances. We return to a discussion of the possible sources of $C_{constant}$ in the next chapter. The isothermal dependence of C_{chem} over the whole pO_2 range is plotted in **Figure 4.12**.

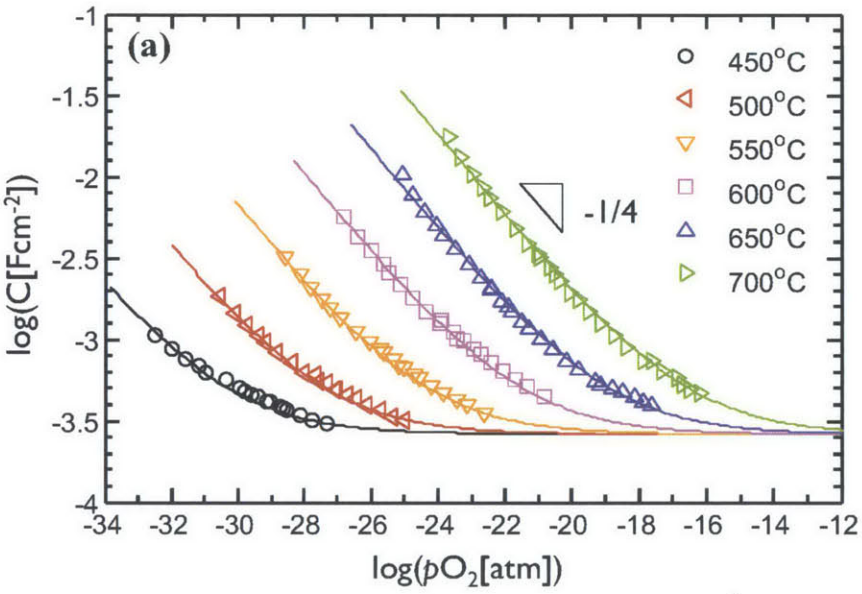

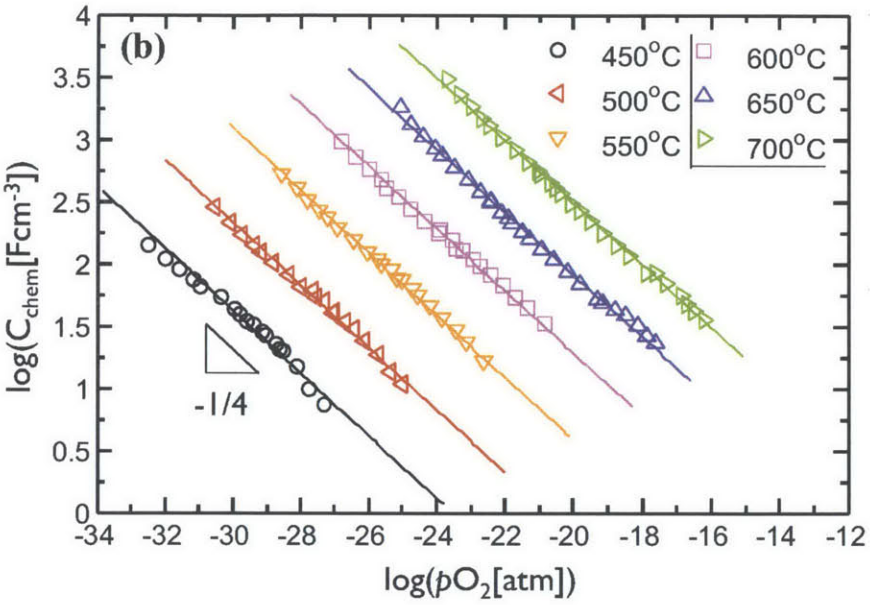

Figure 4.11 (a) Isothermal dependence of the area–specific capacitance on pO_2, obtained from a symmetric PCO/YSZ/PCO cell. Symbols are the measured values. Solid lines represent best fits to Equation (4.4). (b) Isothermal dependence of the volume–specific C_{chem} on pO_2. Solid lines represent best fits to Equation (2.28).

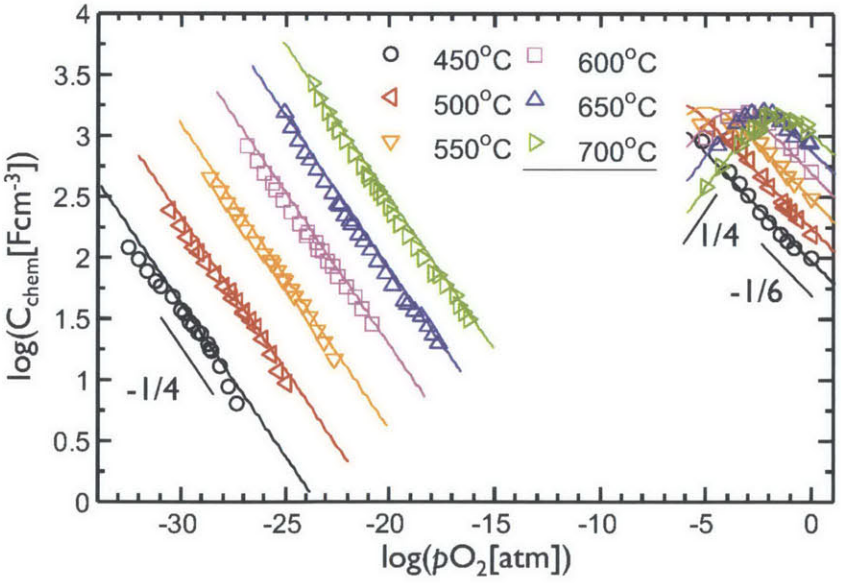

Figure 4.12 Isothermal dependence of the volume–specific C_{chem} on pO_2 over the whole pO_2 region by combing Figure 4.9 and Figure 4.10 (b).

4.5. Bias dependence of EIS

4.5.1. Bias dependence of impedance spectra

Figure 4.13 shows typical impedance spectra obtained at 650°C. The equivalent circuit fits are observed to represent the data well. The origin of each component is discussed in the previous section. Since there is a reference electrode on the YSZ substrate, there is no contribution from the porous Ag electrode. Typical n^q values near unity (0.93 - 1.04 were measured) for Q corresponding to C_{PCO} demonstrate near ideal capacitance.

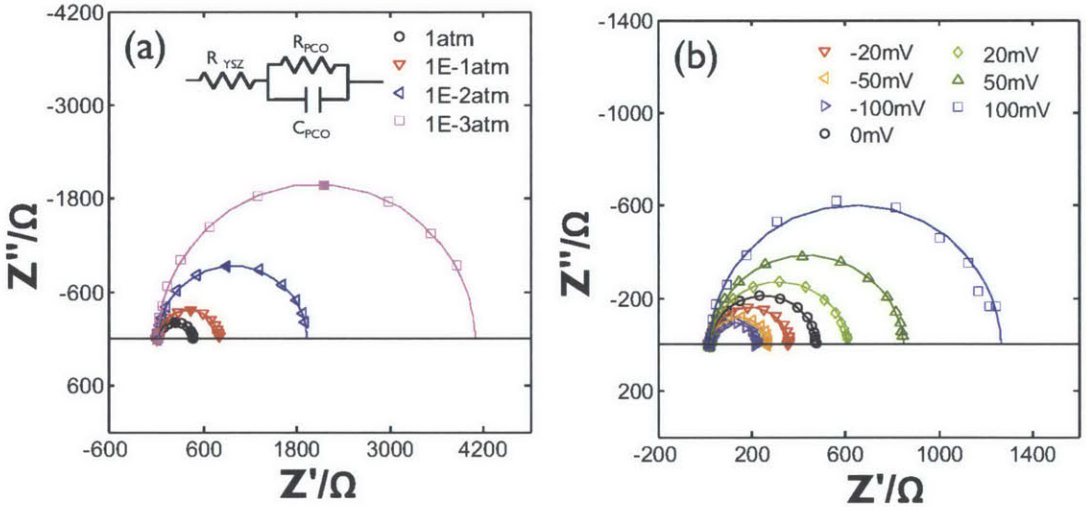

Figure 4.13 (a) Typical impedance spectra collected at 650°C, 0 mV DC bias, at various oxygen partial pressures as indicated. The symbols are the experimental data while the solid lines are the equivalent circuit fit. The filled symbols show the impedance at f= 0.202Hz, 0.080Hz, 0.032Hz, 0.013Hz, respectively, from low pO_2 to high pO_2. The inset shows the equivalent circuit used to fit the data. (b) Typical impedance spectra collected at 650°C, 1 atm pO_2, at various DC biases as indicated. The symbols are the experimental data while the solid lines represent the equivalent circuit fit. Both impedance spectra in (a) and (b) are obtained from a symmetric PCO/YSZ/Ag cell with PCO film thickness of 58 nm.

4.5.2. Bias dependence of C_{chem}

Figure 4.14 (a) summarizes C_{chem} values measured at four different pO_2s (1, 10^{-1}, 10^{-2} and 10^{-3} atm) with either zero bias or with applied voltages, ΔE of ±25, ±50 and ±100 mV. Some clear trends are observed. At zero bias, C_{chem} increases with decreasing pO_2 at 550°C but becomes systematically less sensitive to pO_2 at the lower pO_2 end as temperature increases. This is consistent with what was observed in Figure 4.10. A generally strong dependence of C_{chem} on bias, at a given atmosphere, is observed at 550°C, with C_{chem} increasing with negative bias and decreasing with positive bias. This dependence becomes weaker as temperature is increased, particularly for negative bias conditions. Indeed, at each pO_2, C_{chem} passes through a maximum with the maximum moving towards less negative bias conditions as the temperature increases.

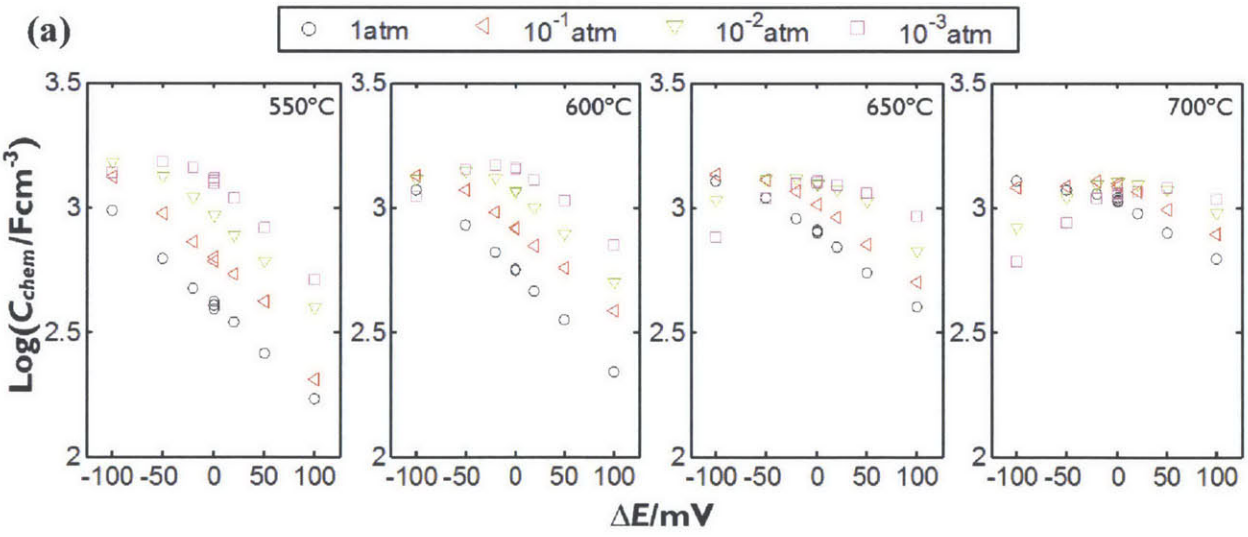

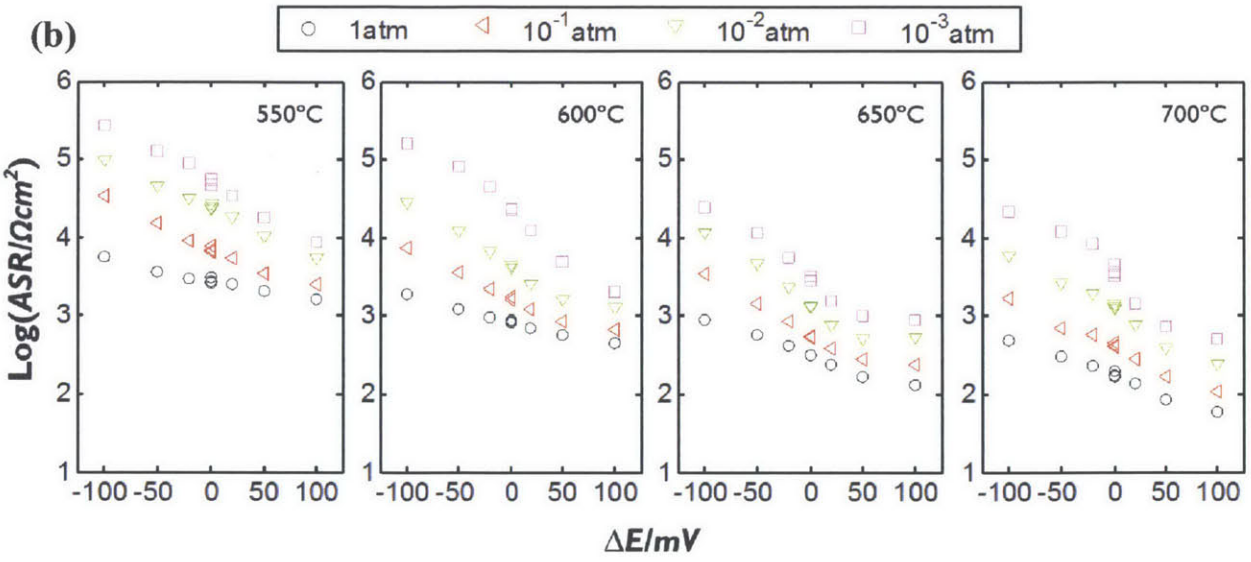

Figure 4.14 Chemical capacitance (a) and *ASR* (b) measured at indicated temperatures as a function of applied voltage at various oxygen partial pressures.

In **Figure 4.15**, the C_{chem} data shown in Figure 4.14 (a) are replotted, at each temperature, as a function of $pO_{2,eff}$ in which ΔE was converted to values of $pO_{2,eff}$ with the aid of Equation (2.31). The filled symbols represent the capacitance measured in equilibrium with the gas phase, i.e., ΔE=0, while the empty symbols represent data obtained under an applied bias ΔE. All the isotherms exhibit a maximum, with the maximum shifting to increasing pO_2, as observed above in which C_{chem} was measured without applied bias.

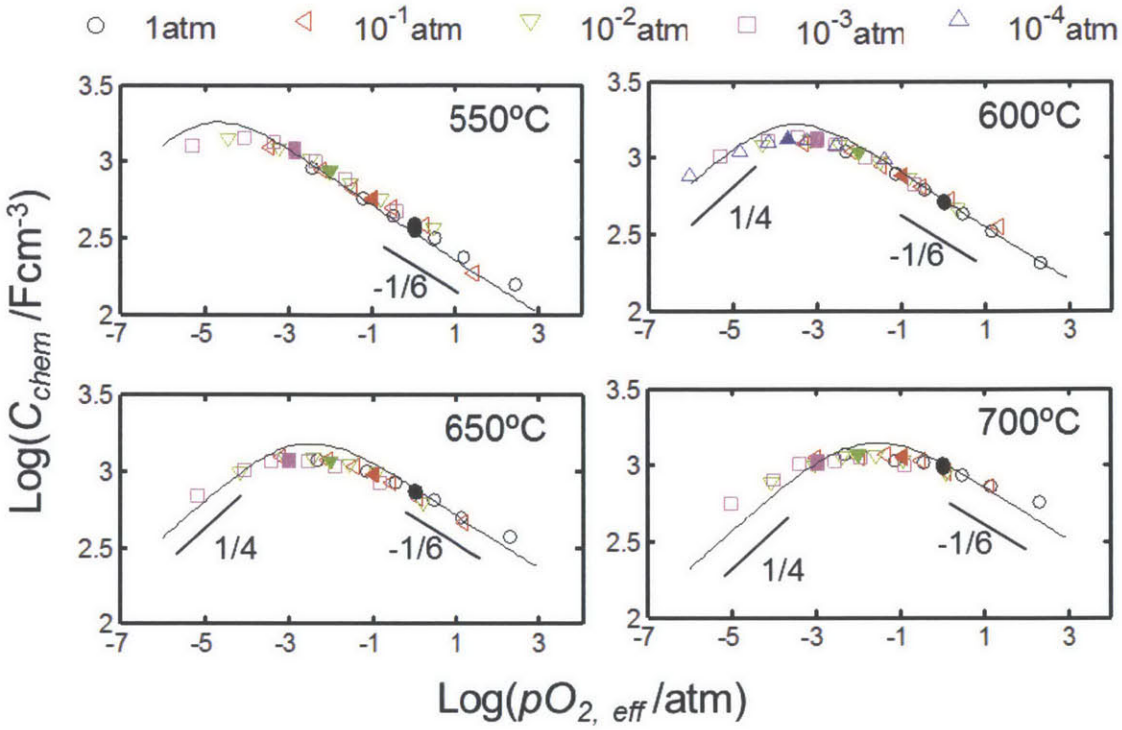

Figure 4.15 Isothermal dependence of volume-specific C_{chem} (symbols) on pO_2, obtained from a PCO/YSZ/Ag cell with PCO film thickness of 58 nm. The filled symbols indicate capacitances measured without applied bias. The empty symbols indicate capacitances when bias was applied. Solid lines represent modeled data.

4.5.3. Bias dependence of R_{PCO}

In **Figure 4.16**, the R_{PCO} data shown in Figure 4.14 (b) are replotted, at each temperature, as a function of $pO_{2,eff}$ in which ΔE was converted to values of $pO_{2,eff}$ with the aid of Equation (2.31). The filled symbols represent the *ASR* measured in equilibrium with the gas phase, i.e., ΔE=0, while the empty symbols represent data obtained under an applied bias ΔE. One observes the *ASR* values, with or without bias, align very well, and have, at best, a weak dependence on the pO_2 in the gas phase.

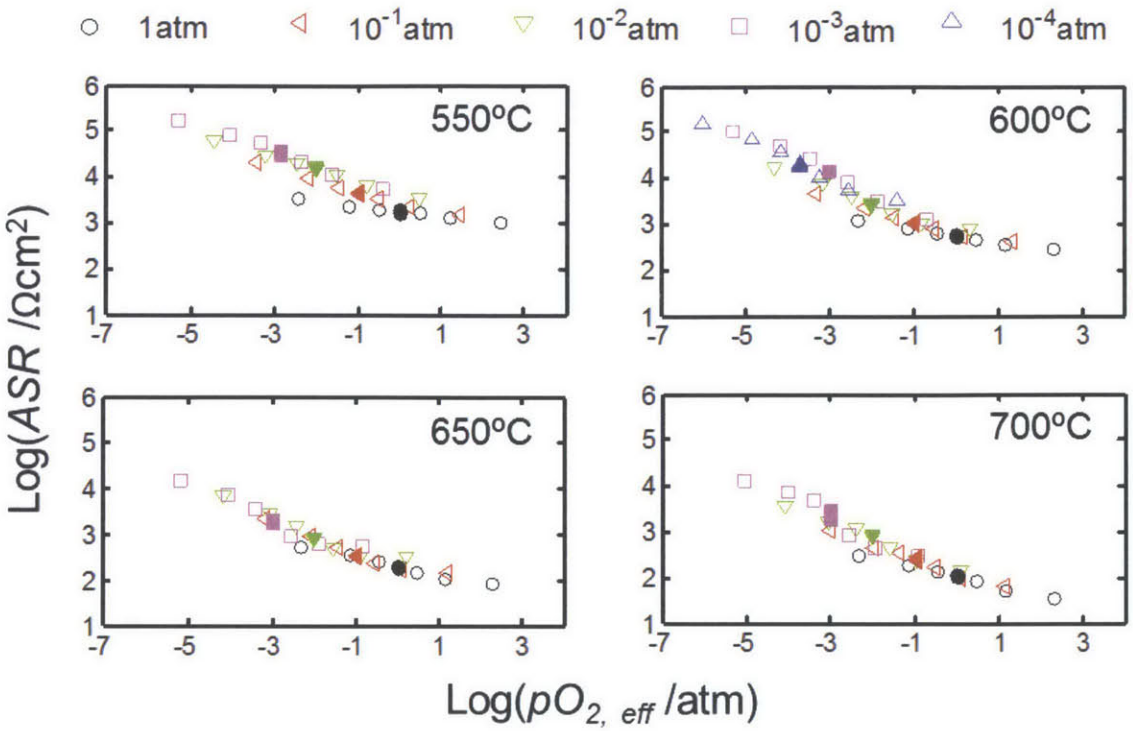

Figure 4.16 Isothermal dependence of area-specific resistance (symbols) on effective pO_2. The filled symbols indicate data when bias = 0mV. The empty symbols indicate data when bias is applied. Data are obtained from a PCO/YSZ/Ag cell with PCO film thickness of 58 nm.

5. CHAPTER 5 DISCUSSION

5.1. Origins of impedance spectroscopy contributions

5.1.1. Origin of R_{off}

Several features of the offset resistance are consistent with the source being the bulk resistance of the YSZ electrolyte single crystal substrate. This includes the activation energy of R_{off} of 1.14 eV and its pO_2 independence (Figure 4.9(b)). Furthermore, the magnitude of the conductivity, calculated based on the present cell electrode geometry, electrolyte thickness and measured R_{off}, agrees well with the literature data of the ionic conductivity of YSZ (Figure 4.9(a)). One can thus confidently conclude that R_{off} simply reflects the YSZ series ohmic contribution to the overall cell impedance.

5.1.2. Origin of R_L and C_L

In an MIEC electrode, three key rate limiting processes need be considered for oxygen transport from the gas phase into the dense electrode and ultimately into the electrolyte [5]. These are (i) oxygen surface exchange at the electrode-gas interface, (ii) mass transport through the electrode, and (iii) transfer of oxygen ions across the PCO/YSZ interface. In electrodes like $La_{1-x}Sr_xMnO_3$, which are not significant MIECs (i.e. they display predominant electronic with minimal ionic conduction), oxygen reduction and insertion is limited to the triple phase boundary (TPB) between electrode, electrolyte, and gas phase as is the rate of diffusion through the electrode (**Figure 5.1**) [91]. The oxygen insertion process will have different dependencies on electrode geometry depending on whether, for example, the exchange reaction is limited to the TPB or can occur anywhere along the 2 phase boundary (electrode surface) as would be the case for a mixed conductor. In addition, reaction products can form at the electrode/electrolyte

interface, blocking ion transport [92]. As the use of dense thin-film electrodes enables one to easily control geometry, one can more readily deduce the dominant reaction site(s) by obtaining a quantitative relationship between electrode impedance and geometry. These relationships are summarized in **Table 5.1**.

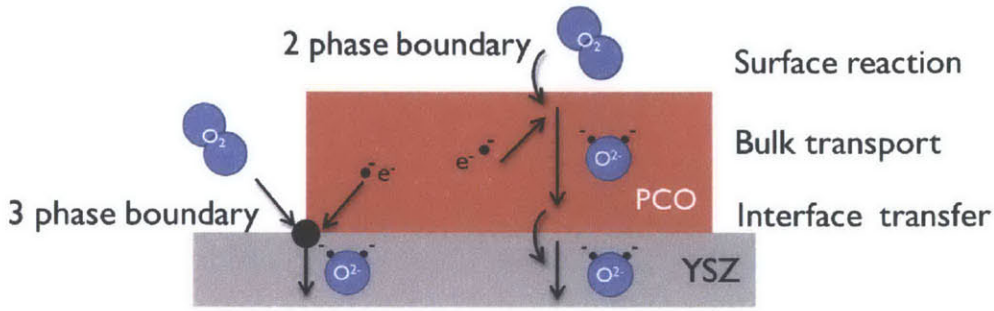

Figure 5.1 Typical dominant reaction paths for oxygen reduction on MIEC (2-phase boundary) and non MIEC (3 phase boundary) electrodes.

Table 5.1 Possible origin of R_{PCO} and its geometric dependences

	Surface Area (S)	Film Thickness (h)
Surface exchange	$R \propto S^{-1}$	$R \propto h^{0}$
Bulk transport	$R \propto S^{-1}$	$R \propto h^{1}$
TPB	$R \propto S^{-1/2}$	$R \propto h^{0}$

From the linear dependence of R_L (= R_{PCO}) on surface area (Figure 4.4), one can conclude that the oxygen reduction reaction occurs over the full electrode surface area of PCO, rather than being limited to the TPB (see Table 5.1), as also reported for thin-film $SrTi_xFe_{1-x}O_{3-\delta}$ (STF) [93], $La_{1-x}Sr_xCoO_{3-\delta}$ (LSC), and $La_{1-x}Sr_xCo_{1-y}Fe_yO_{3-\delta}$ (LSCF) [94] MIEC electrodes. From the thickness independence of the R_{PCO} (Figure 4.6), one can confirm that oxygen diffusion through the film (Bulk transport in Table 5.1) is not controlling the electrode response. Lastly, a blocking tertiary

phase is not expected (nor observed via XRD) at the electrode/electrolyte interface since both YSZ and PCO exhibit the fluorite structure. Indeed other studies intentionally use doped ceria as a protective buffer layer to avoid a reaction product to form between, for example, LSC and YSZ [95][94]. Thus, one can confidently conclude that R_{PCO} is limited by surface exchange kinetics for all three PCO compositions studied here.

Next, turning to C_L (=C_{PCO}) in Figure 4.3, it too has different possible origins. These are (i) bulk capacitance, (ii) capacitance at the electrode-electrolyte interface, and (iii) defect concentration dependent chemical capacitance. As in the resistance study, one can also deduce the type of capacitance by controlling the sample geometry (**Table 5.2**).

Table 5.2 Possible origin of C_{PCO} and its geometry dependence

	Surface Area S	Film Thickness h
Bulk capacitance	$C \propto S^1$	$C \propto h^{-1}$
Interfacial capacitance	$C \propto S^1$	$C \propto h^0$
Chemical capacitance	$C \propto S^1$	$C \propto h^1$

Log C_{PCO} for PCO10 is plotted vs. log S in Figure 4.5 and shows a power law dependence of 1. In Figure 4.7, log C_{PCO} is plotted vs. log h, and shows a power law dependence of 1. Both of these results point to the capacitance as being "chemical capacitance". The fact that the fitted line in Figure 4.7 passes through the origin, further confirms the absence of measurable interfacial capacitance contributions (interface capacitance typically results in an offset on the y axis of Figure 4.7 [77]). PCO1 and PCO20 show a similar geometrical dependence of capacitance on h and S as does PCO10. Additionally, the C_{PCO} values are orders of magnitude higher than

typical interfacial capacitances, e.g. 25.0 mF/cm^2 for a 333.4 nm thick PCO10 film at 670 °C (typical n value between 0.979 and 0.997, see Equation (4.2)), in agreement with the magnitude of chemical capacitance reported in other thin film MIEC systems [96][93].

5.2. Surface exchange of PCO films

5.2.1. Values for the area specific resistance (ASR) and surface exchange coefficient (k^q)

Since the surface exchange reaction has been identified as being the rate limiting process for oxygen exchange, the corresponding surface exchange rate coefficient can now be extracted from the measured electrode resistance. Previously, the electrically derived surface oxygen exchange coefficient (k^q) has been defined as inversely proportional to the resistance as [97]

$$k^q = \frac{kT}{4e^2 R_S c_O} \tag{5.1}$$

where k is the Boltzmann constant, e is the electron charge, T is the temperature, Rs is the area specific resistance (equal to R_{PCO}), and c_O is the total concentration of lattice oxygen (~5.04×10^{22} cm^{-3}).

Calculated k^q values are listed in **Table 5.3**. Further confirmation of surface exchange control can be obtained by examining the so-called characteristic thickness L_C, the ratio of the oxygen diffusion coefficient and the corresponding surface exchange coefficient, $L_C = D/k^q$ [98], above which mass transport through the electrode thickness becomes dominant relative to the surface exchange reaction [98]. Values for the oxygen diffusion coefficient are derived from an analysis of electrical conductivity measurements performed on PCO [99]. The characteristic thickness of PCO10 and PCO20 at 670°C is approximately 3.58×10^5 and 2.20×10^5 μm, respectively, orders of magnitude thicker than the PCO film thicknesses used in this work.

Furthermore because L_C becomes thicker with decreasing temperature, given the larger activation energy of k^q than D, it is clear that the surface exchange reaction remains dominant in the temperature range of 550–670°C.

Table 5.3 Surface exchange coefficient, oxygen diffusion coefficient and characteristic thickness of PCO with different Pr concentrations.

	k^q (cm/s)	D (cm^2/s)	L_c (μm)
PCO1	1.38×10^{-8}	2.31×10^{-9}	1.68×10^{5}
PCO10	3.73×10^{-8}	1.34×10^{-8}	3.58×10^{5}
PCO20	4.59×10^{-8}	1.01×10^{-8}	2.20×10^{5}

Table 5.4 Surface exchange coefficient, electronic and ionic conductivity, and electronic transfer numbers at 800°C in air (k^q for PCO are extrapolated to high temperature, enabling comparison with STF and LSCF).

	k^q (cm/s)	σ_{el} (S/cm)	σ_{ion} (S/cm)	t_e
PCO1	1.02×10^{-7}	2.91×10^{-5}	3.21×10^{-3}	0.009
PCO10	3.90×10^{-7}	1.73×10^{-2}	2.64×10^{-2}	0.396
PCO20	4.75×10^{-7}	3.48×10^{-2}	1.89×10^{-2}	0.648
$SrTi_{0.5}Fe_{0.5}O_{3-\delta}$[32][26]	1.7×10^{-5}	1.8	3.6×10^{-2}	0.9804
$La_{0.6}Sr_{0.4}Co_{0.2}Fe_{0.8}O_3$[33]	5.6×10^{-6}	3.02×10^{2}	8×10^{-3}	0.9997

R_S and k^q obtained for dense thin films of other MIEC electrodes prepared by PLD are compared in **Figure 5.3** with those of PCO, helping to ensure that morphology differences between typical bulk MIEC electrodes, and the dense thin film PCO electrodes used in this study, played no role in influencing comparison of performance. The R_S and k^q values for PCO are

comparable with those of LSC, LSCF and STF, particularly at temperatures below 700°C, pointing to the suitability of PCO as a realistic model MIEC cathode material. Interestingly, as shown in **Table 5.4**, PCO displays high k^q values despite having a considerably lower electronic conductivity than the previously listed cathode materials (a high value is often suggested as a necessity for high k^q [68]). The origin of this unexpected phenomenon needs further investigation.

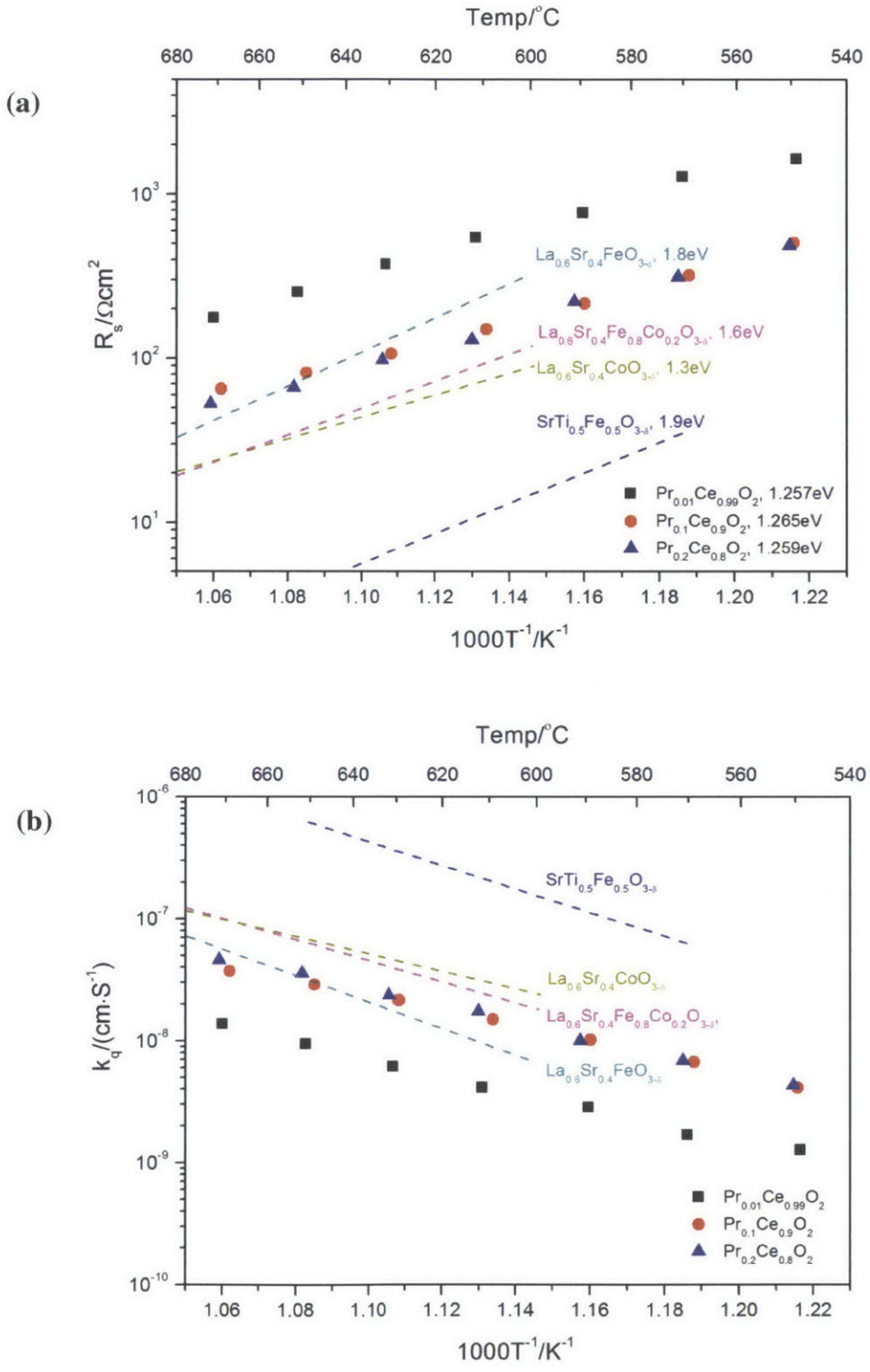

Figure 5.2 Temperature dependence of $R_S = R_{PCO}$ (a) and k^q (b) of PCO compared with other dense thin-film MIEC electrodes fabricated by PLD: $La_{0.6}Sr_{0.4}FeO_{3-\delta}$ [94], $La_{0.6}Sr_{0.4}Fe_{0.8}Co_{0.2}O_{3-\delta}$ [94], $La_{0.6}Sr_{0.4}CoO_{3-\delta}$ [94] and $SrTi_{0.5}Fe_{0.5}O_{3-\delta}$ [93].

5.2.2. Temperature and $pO2$ dependence of R_{PCO}

The activation energies (E_A) derived from, the Arrhenius dependence of R on reciprocal temperature

$$R = R_{\circ} \exp(-E_A / kT) \tag{5.2}$$

for PCO1, PCO10, and PCO20 in air for temperatures from 550°C to 670°C are compared with other MIEC materials in Figure 5.2 (a) and are as a group found to range from approximately 1.3 to 1.9 eV. Those for PCO, ~1.3 eV, are closest to that of LSC.

The pO_2 dependence of the electrode resistance is shown in **Figure 5.3** in the form of a log-log plot. The slope is close to -1/3 at high pO_2 and close to -1 at low pO_2. This implies a mechanism change between the two regions. A similar shift in pO_2 dependence of the electrode resistance in the $SrTi_{1-x}Fe_xO_{3-\delta}$ was ascribed to a shift from charge transfer control at high pO_2 to the availability of adsorbed oxygen species at low pO_2 [100].

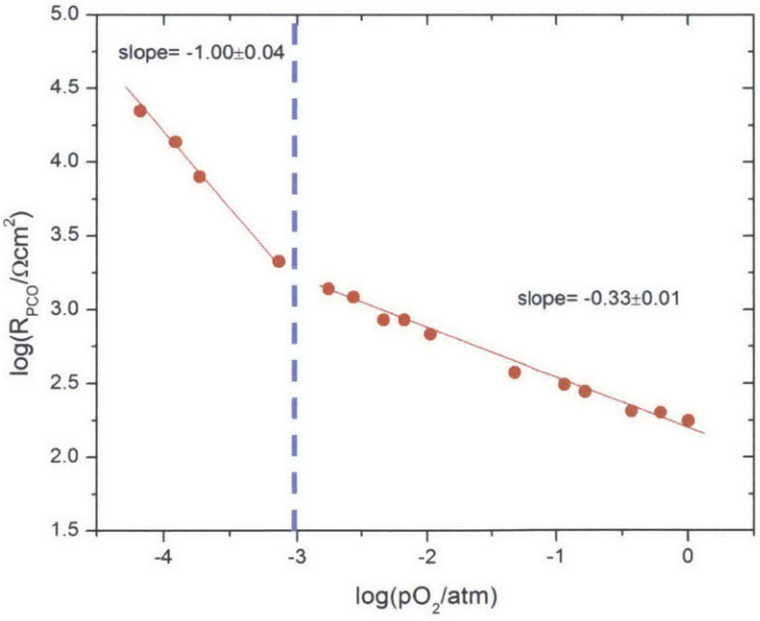

Figure 5.3 pO_2 dependence of R_{PCO} of PCO10 at 670°C. The pO_2 at which an apparent transition in rate limiting mechanism occurs is indicated by the vertical dashed line.

5.3. Analysis of chemical capacitance (C_{chem})

5.3.1. Estimation of non-stoichiometry using C_{chem}

In Figure 2.1, the power law dependence of C_{chem} has been predicted in five regions, from high pO_2 to low pO_2. This dependence is clearly visible in the experimental results, as showing in Figure 4.11, allowing for the extraction of $[V_O^{\bullet\bullet}](pO_2^{\circ})$ directly from measurements of C_{chem}. By applying Equation (2.15) with the aid of Equation (2.20) and (2.25), and Equation (2.29), to the C_{chem} data in Figure 4.11, we were able derive the dependence of the oxygen vacancy concentration, and thereby the oxygen non-stoichiometry, as functions of temperature and pO_2. The results are shown in **Figure 5.4** (open symbols for low pO_2, filled symbols for high pO_2). The data show little scatter, demonstrating the relatively high precision attainable by this electrical impedance method as compared with typical TGA or coulometric titration measurements.

The inset in Figure 5.4 shows the change in non-stoichiometry, log (δ– 0.05) at low pO_2, which displays the expected -1/4 power law based on the dilute solution approximation. In the absence of defect association, ceria is predicted to display a -1/6 slope at even lower pO_2, as the vacancy concentration formed by reduction of ceria exceeds that of the dopant. This -1/4 slope implies that defect association, while expected [101],[102], is not substantially impacting the generation of the small excess of oxygen vacancies due to reduction.

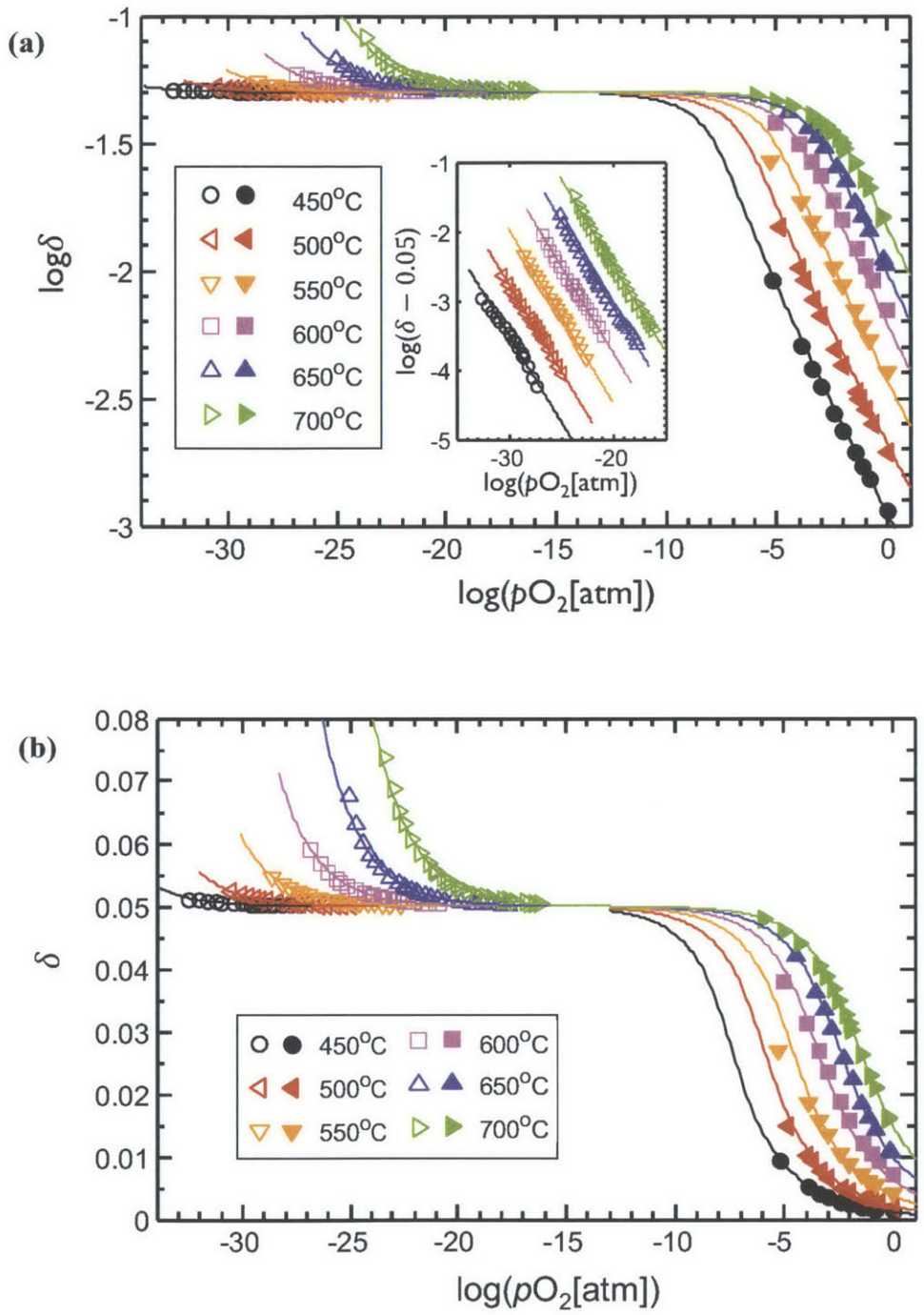

Figure 5.4 Log (a) and linear (b) non-stoichiometry of thin film PCO vs log pO_2 as derived from C_{chem}, from this work, at low pO_2 (empty symbols) and at high pO_2 (filled symbols)[103], respectively. Solid lines represent best fits to the defect model. The plateau represents δ=0.05, where Pr^{4+} is fully reduced to Pr^{3+}. Inset in (a) shows log (δ-0.05) vs. log pO_2.

5.3.2. Derivation of defect equilibrium model parameters

By fitting the PCO defect model to the δ values extracted from C_{chem}, the defect formation parameters could be derived and compared to those published earlier for bulk PCO, see **Table 5.5**. One observes that the parameters derived from the thin film chemical capacitance data are close to values derived for bulk $Pr_{0.1}Ce_{0.9}O_{2-\delta}$. It is interesting to note that the enthalpy for reduction $H^{\circ}_{r,Pr}$ while nominally smaller for the film, is equal to that of the bulk taking into account the margin of error reported for the two values. From these results, one would conclude that the thermodynamic parameters for PCO change little with respect to the bulk, within experimental error, when prepared in the present thin film geometry.

Table 5.5 Parameters used in the defect equilibrium model for $Pr_{0.1}Ce_{0.9}O_{2-\delta}$. Thin film parameters are determined from C_{chem}. Bulk parameters are determined from TGA. $[Pr_{0.1}Ce_{0.9}O_{2-\delta}] = 2.52\times10^{22}$ cm^{-3} for density=7.21g·cm^{-3} [20].

	Thin film	Thin film (bias control)	Bulk[20]
$H^{\circ}_{r,Pr}$, eV	1.80±0.04	1.79	1.90±0.07
H°_{r}, eV	4.13 ± 0.08		4.76±0.04
H_{Pr}, eV	-1.17 ± 0.06		-1.43±0.03
f, eV·δ^{-1}	-6.2±1.5	-4.5	-4.63±1.9
$k^{\circ}_{r,Pr}$, atm$^{1/2}$	(0.90±0.60)×10^{6}	1.17×10^{6}	(2.114±1.23)×10^{6}

Values of δ form the PCO10 film are compared with data obtained for bulk PCO measured by TGA as well as values calculated from the defect model using the parameters listed in **Table 5.5**. First, one notes that the experimental data agree well with the trends and absolute values observed for the defect model, derived by fitting δ for the film, demonstrating the utility of chemical capacitance in deriving reliable non-stoichiometry data for ceria based thin films.

Second, the film exhibits a small but systematic shift from the bulk data in the direction of larger δ values for the same temperature and pO_2 conditions.

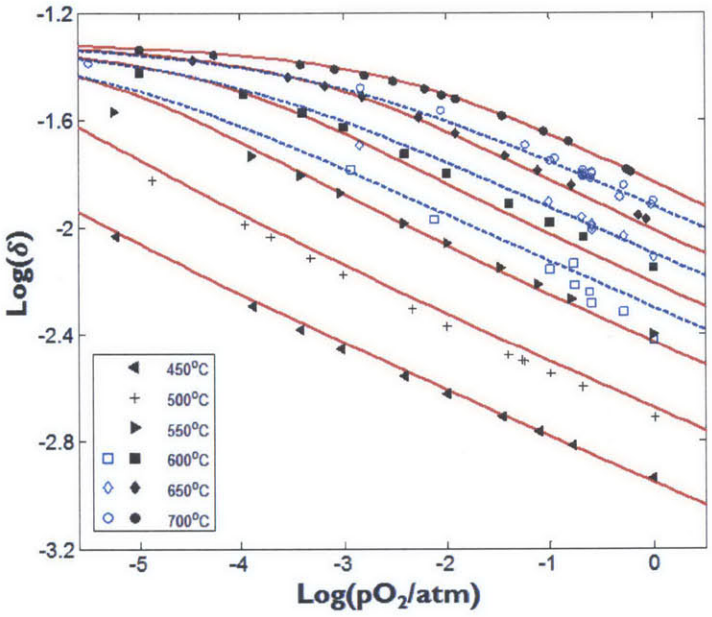

Figure 5.5 Non-stoichiometry of thin film and bulk PCO derived from C_{chem} (filled symbols) and TGA (empty symbols), respectively.[18] The solid and dashed lines represent δ for thin films and bulk, respectively, calculated from the defect model using the parameters listed in Table 5.5.

The question remains why bulk and thin film non-stoichiometry data match well for ceria thin films but not for the mixed conducting perovskite $La_{1-x}Sr_xCoO_{3-\delta}$ reported to date. For example, Kawada et al. reported a 45% increase in reduction enthalpy for LSC, whereas in the present case only a 5% decrease, within the margin of error, is observed here for PCO.[27] While others have suggested that strain, induced either by lattice mismatch or thermal expansion mismatch between substrate and film, may be playing a role, [27] an alternate explanation, based on the known reactivity of many of the perovskite oxide films with YSZ, [92] may also play a role. Along these lines, one may also note the heavy segregation of Sr to the surfaces of the perovskite

films, leading to large compositional changes, at least in the vicinity of the surface.[104,105] To date, no evidence for significant Pr segregation to the surface in PCO, nor reaction with the YSZ substrate, has been observed, nor is expected.

5.3.3. The background capacitance ($C_{constant}$) at low pO_2

Briefly turning back to $C_{constant}$, prior investigators have suggested the existence of an interfacial capacitance tied to the defect concentration and bulk permittivity of the material through the following Equation (5.3) below [74][106].

$$C_{ion,2PB}^{gas} \approx \sqrt{\frac{4\varepsilon\varepsilon_{\circ}e^{2}[V_{O}^{\bullet\bullet}]}{kT}} \tag{5.3}$$

Since the total oxygen vacancy concentration is largely pO_2 independent in the region where $C_{constant}$ is significant, the interfacial capacitance would be predicted to be nearly constant as well. Inputting values for the parameters in Equation (15) yields values of C_{ion}=2.66-8.41×10^{-4} F·cm^{-2} for temperatures of 450°C-700°C, respectively. These calculated values match closely those derived experimentally (~3×10^{-4} F·cm^{-2}). It should be noted, however, that this does not take into account the possible influence of surface defect concentrations, which in other studies has been suggested to differ substantially from that of the bulk [101] [107].

5.4. Study of impedance under bias

5.4.1. Using bias to control the non-stoichiometry of PCO films

The isothermal dependence of volume-specific C_{chem} (symbols) on pO_2, with or without bias, is shown in Figure 4.15. All isotherms exhibit a maximum. Returning to the definition of C_{chem} given in Equation (2.14), this simply corresponds to the condition at which the rate of change in oxygen vacancy concentration or δ with change in pO_2 is at its peak. Also included in

the figure, as s solid curve, are calculated values of C_{chem} derived from the defect equilibrium model that provides for the prediction of $[V_O^{\bullet\bullet}]$ as functions of temperature and pO_2. One observes a good fit between the predicted and measured values of C_{chem}, whether obtained with or without bias.

Figure 5.6 shows the δ values extracted from C_{chem}, derived with the aid of Equation (2.20) and (2.15), as a function of $pO_{2,eff}$ for a series of isotherms ranging from 550 to 700°C. The results are compared to δ values with parameters listed in **Table 5.5** (dash lines). First, one observes excellent registry and little scatter between δ values derived from C_{chem}, with and without DC bias. This points to the effectiveness of bias in controlling non-stoichiometry in PCO films. Second, δ values extracted from C_{chem} match well with those predicted from the defect model. The only significant deviation occurs at the lowest isotherm of 550°C, wherein the experimental data show a slightly steeper dependence on pO_2, which may reflect the greater difficulty in reaching equilibrium at lower temperatures [108]. These results confirm the suitability of using bias across an electrochemical cell to conveniently and precisely control δ of oxide thin films in an in-situ fashion and simultaneously monitor these changes by measurement of the chemical capacitance.

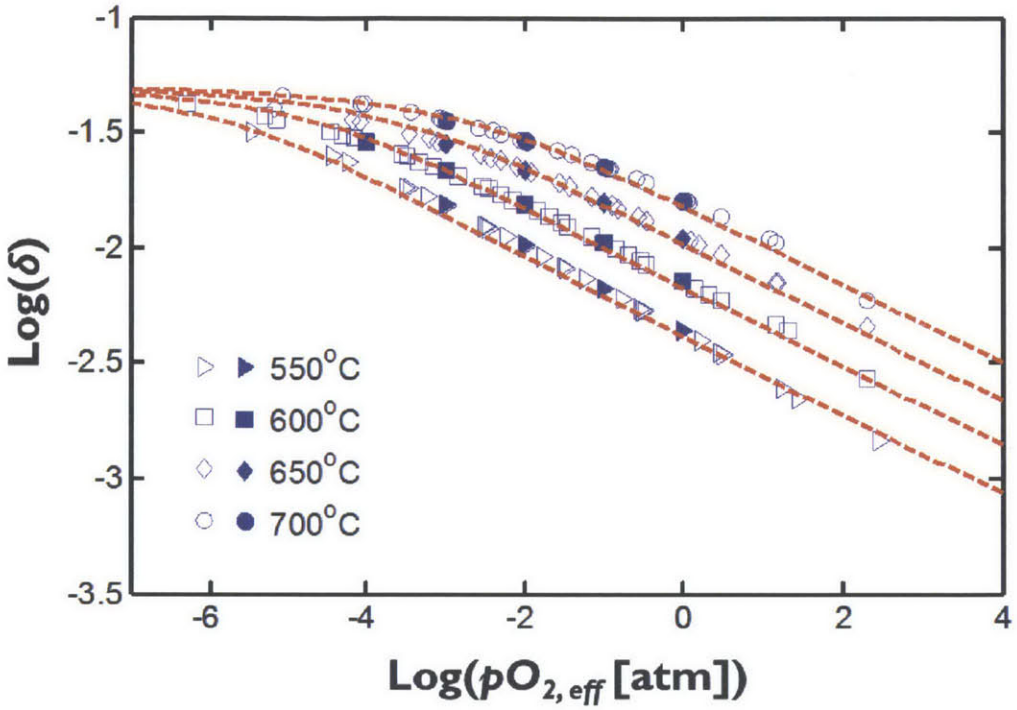

Figure 5.6 Isothermal dependence of non-stoichiometry (symbols) on pO_2, calculated from C_{chem} in Figure 4.5. The filled symbols indicate non-stoichiometry when bias = 0 mV. The empty symbols indicate capacitances when bias is applied. Dash lines represent modeled data.

Another unusual feature of utilizing bias to access higher and lower oxygen activities than those existing in the surrounding gas phase, is the possibility of achieving oxygen activities very difficult to achieve experimentally otherwise. Specifically, one can notice by observation of Figures 5.6, that values of $pO_{2,eff}$ as high as 280 atm were achieved by application of a positive bias of 100 mV with a much simpler experimental apparatus than used in previous studies [21–23]. Interestingly, the data collected for $pO_{2,eff}$ values above 1 atm appear to continue to fit the predicted model quite well even though, at these high oxygen activities, on would expect to have to replace concentrations with activities.

As we discussed in the introduction, many properties of the oxide are strong functions of δ. By control of δ by DC bias, these properties can, in principle, be tuned. Possible applications

could be for controlling properties of magnetic thin film memory devices[109] and the thermal conductivity in oxide thin films [10].

5.5. Using bias to study the Oxygen Reduction Reaction (ORR) of PCO films

The correlation between pO_2 and *ASR* has been studied by various groups as a means for investigating the ORR mechanisms operative on the electrode surface. In most experiments, the oxygen activity is controlled by controlling the pO_2 in the gas phase ($pO_{2,\,gas}$). However, when $pO_{2,\,gas}$ changes, the defect species in the film and adsorbed gas species on the surface change their concentrations accordingly. This makes it hard to isolate the decisive factor. In this study, $pO_{2,\,gas}$ is controlled by adjusting the flow rate of the mass flow controllers, while the effective pO_2 in the electrode ($pO_{2,eff}$) is controlled by applying bias to the electrode. In the meantime, the defect concentrations in the film are measured in-situ by C_{chem}. This configuration allows one to tune the $pO_{2,\,gas}$ and $pO_{2,\,eff}$ independently, and test their impacts on *ASR* separately for the first time.

The $pO_{2,\,eff}$ dependence of *ASR* measured under different $pO_{2,\,gas}$ is presented in Figure 4.16. Here we replotted the data at 650°C in **Figure 5.7**. At other temperatures the results are similar. In Figure 5.7, the filled symbols indicate data when bias = 0 mV, while the empty symbols indicate data when bias is applied. First we note the strong dependence of log ASR on log $pO_{2,\,eff}$ with ASR decreasing with increasing $pO_{2,\,eff,}$ as is typical for most oxide cathodes. Clearly, *ASR* values can be shifted from values measured under specific $pO_{2,\,gas}$ by application of bias, but still consistent with expectatios based on $pO_{2,eff}$. This means the *ASR* is fixed by $pO_{2,\,eff}$ rather than $pO_{2,\,gas}$. Since the oxygen molecule absorption onto the PCO surface depends on $pO_{2,\,gas,}$ this result suggests that the oxygen molecule absorption onto the PCO surface may not the rate limiting step, assuming that oxygen adsorption is not impacted by $pO_{2,\,eff.}$

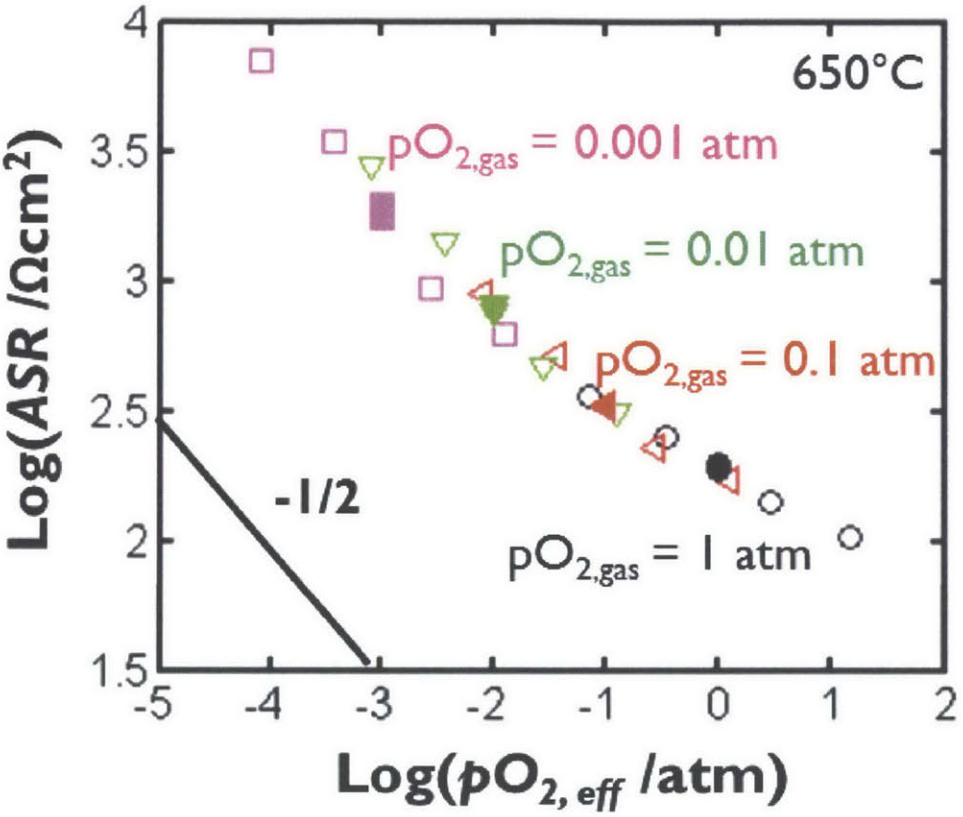

Figure 5.7 Isothermal dependence of area-specific resistance (*ASR*) on effective pO_2 at 650°C. The filled symbols indicate data when bias = 0 mV. The empty symbols indicate data when bias is applied. Data are obtained from a PCO/YSZ/Ag cell with PCO film thickness of 58 nm.

With the δ of the PCO film obtained from C_{chem}, one can plot the isothermal dependence of *ASR* on δ, as shown in **Figure 5.8**. Several features can be observed: (1) *ASR* values measured under different $pO_{2,\,gas}$ align well on a universal curve, as long as δ is kept the same. (2) *ASR* increases with increasing δ. When δ increases by one order of magnitude, *ASR* increased by more than two orders of magnitudes. (3) The slope becomes steeper as δ increases.

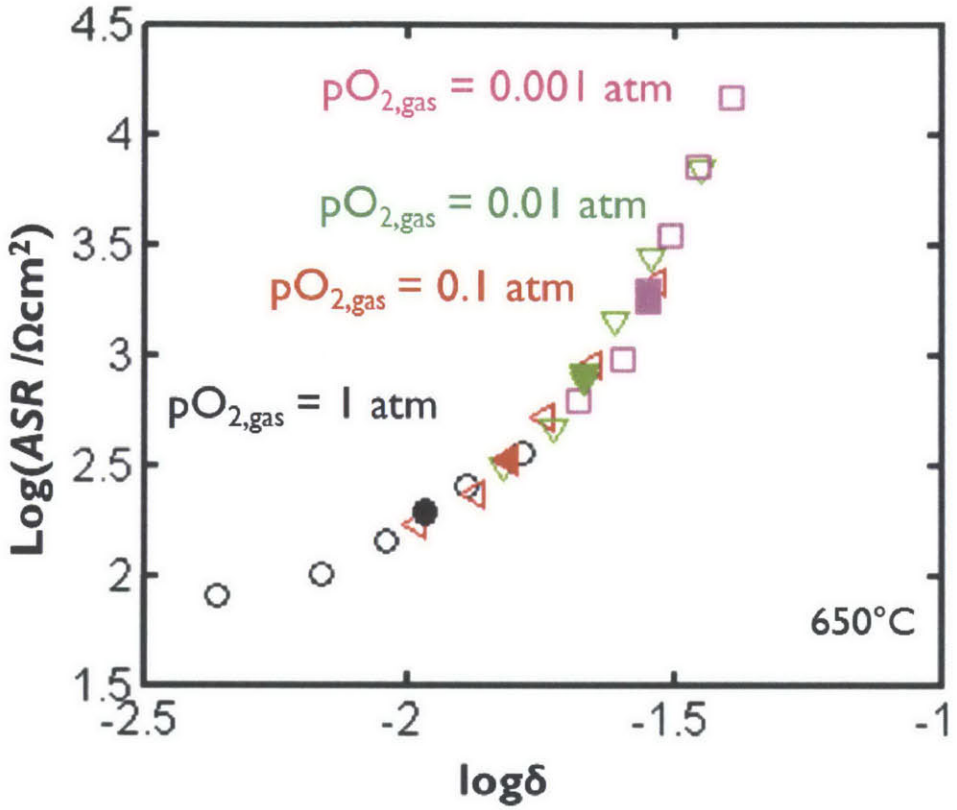

Figure 5.8 Isothermal dependence of area-specific resistance (*ASR*) on δ at 650°C. The filled symbols indicate data when bias = 0mV. The empty symbols indicate data when bias is applied. Data are obtained from a PCO/YSZ/Ag cell with PCO film thickness of 58 nm.

In PCO at high pO_2 region, n and $[V_O^{\bullet\bullet}]$ increase with increasing δ, while p decreases with increasing δ. One can plot the dependence of surface exchange rate k and defect concentrations on δ, as showing in **Figure 5.9**. This figure can serve to clarify the rate determine step of the cathode reaction. These trends seem counter intuitive and in conflict with proposed models in the literature. First observation: 1) When $[V_O^{\bullet\bullet}]$ increases, k decreases. This is opposite to what Kuklja et al. found in the LSM system[110] and Wang et al. found in BSCF system[111], in which the k^q was proportional to the vacancy concentration. These authors proposed that the vacancy transfer is the rate determine step, and that the product of vacancy concentration and oxygen

diffusivity, $[V_O^{\cdot\cdot}]D_O$ in LSM and BSCF systems, is rate controlling. However, the vacancy concentration is high in PCO. 2) When n increases, k decreases. This is opposite to what Jung et al. found in the STF system, in which they postulated that electron charge transfer at high pO_2 was limiting[43]. This leaves only the hole concentration as limiting oxygen exchange, not normally identified as the rate limiting step.

In considering the unusual conclusions deriving from the results of **Figure 5.8** and **5.9**, one should keep in mind that the PCO system differs substantially from the perovskite cathode materials in the much reduced electronic conductivity and lack of p-type character. Indeed, the electronic conductivity in PCO comes largely from electron hopping within the Pr impurity band. This may therefore have a marked effect on the electrode kinetics. Future work now needs to be done to understand the detailed reaction mechanism controlling electrode kinetics in PCO. Nevertheless, the author has shown the possibility of separately controlling the non-stoichiometry and thereby the concentration and makeup of the defects in oxide electrode thin films with the potential, thereby, to isolate the key contributions to electrode kinetics.

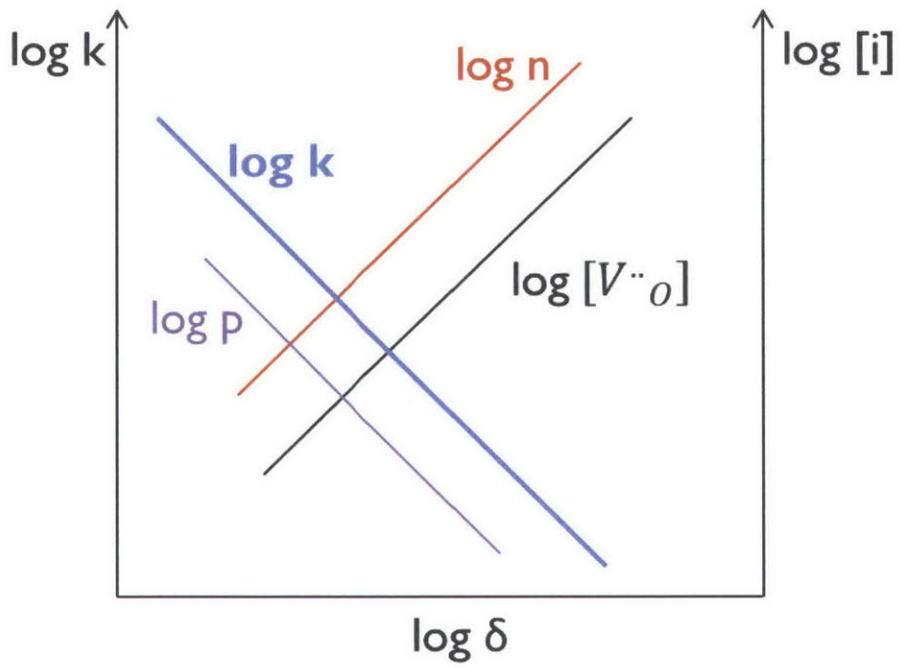

Figure 5.9 The dependence of surface exchange rate k and defect concentrations on δ.

6. CHAPTER 6 CONCLUSIONS

6.1. Summary

In this dissertation I described a method of utilizing the chemical capacitance (C_{chem}) and DC bias to both measure and control the non-stoichiometry (δ) of oxide thin films. I demonstrated that this method can be used to study the defect chemistry of oxide thin films, control the materials properties that are coupled to the nature and concentration of the dominant defect species and to aid in elucidating the correlation between the defect concentrations in the film and oxygen reduction reaction kinetics under cathodic operating conditions representative of those used in Solid Oxide Fuel Cells (SOFC).

The chemical capacitance of $Pr_{0.1}Ce_{0.9}O_{2-\delta}$ (PCO10) thin films, deposited onto single crystal YSZ substrates, was extracted from measured impedance data and used to obtain values for δ as a function of temperature and pO_2. Thermodynamic parameters, describing defect generation in PCO, were derived and found to be in close agreement with those obtained for bulk PCO, demonstrating the utility of chemical capacitance in deriving reliable non-stoichiometry data for ceria based thin films. Approximations, relating chemical capacitance directly to oxygen vacancy concentration, without a fitting parameter, were derived in key defect regimes, thus allowing extraction of the absolute values of δ for specific ranges of pO_2 and temperature. The films were found to reduce more readily than the bulk counterparts.

DC bias was successfully used to control δ of a PCO thin film over a wide temperature and pO_2 range (550 to 700°C, 10^{-4} atm to 1 atm). δ values, calculated from C_{chem}, agree well with those predicted by the defect chemical model, confirming the suitability of using bias to conveniently and accurately control the δ of oxide thin films. This technique provides additional

flexibility in enabling access to oxygen activities difficult to achieve by conventional means, e.g. oxygen pressures of up to 280 atm, and also in small increments. .

The surface exchange coefficient, k, was found to be dependent on the oxygen activity and thereby the oxygen non-stoichiometry δ within the PCO film. The observed dependence implied a decrease in k with increasing $[V_O^{\bullet\bullet}]$ and n and decreasing p, contrary to conclusions found in most perovskite-based oxide cathodes. This may be related to the much lower electronic conductivity found in PCO. Further studies are recommended to examine these findings in greater detail.

6.2. Recommendations for Future Work

There are a number of questions raised by this work. The following are some of the more promising avenues recommended for future study:

- This study demonstrated the suitability of chemical capacitance for deriving reliable non-stoichiometry data for fluorite thin films. However, in earlier studies performed on perovskite films, poor correlations were found between chemical capacitance and TGA or coulometrically derived values for δ. This may be due to chemical reactions between the perovskite films and the underlying YSZ substrate or compositional changes in the films related to segregation effects. Further investigations can perform similar studies on perovskite oxide films. However, the film/substrate and film/gas interfaces should be carefully examined to ensure that they are compositionally correct and/or appropriate buffer layers be applied to restrict reactions.
- This study demonstrated a way of using DC bias to conveniently and precisely control the non-stoichiometry of oxide thin films. Further studies could utilize this technique to

control various other film properties (for example, thermal conductivity[10], optical absorptivity[7], magnetic permeability, chemical expansion[112], etc.) of oxide thin films.

- This study demonstrated a new technique to study the rate determining step (RDS) in the ORR at cathodes. Since the RDS heavily depends on the materials system, similar investigations should be performed on other SOFC electrode materials.

REFERENCES

[1] M. K. Nowotny, T. Bak, J. Nowotny, *J. Phys. Chem. B* **2006**, *110*, 16270.

[2] F. C. Voogt, T. Hibma, G. L. Zhang, M. Hoefman, L. Niesen, *Surf. Sci.* **1995**, *331–333, P*, 1508.

[3] A. Rothschild, W. Menesklou, H. L. Tuller, E. Ivers-Tiffée, *Chem. Mater.* **2006**, *18*, 3651.

[4] H. L. Tuller, *J. Electrochem. Soc.* **1979**, *126*, 209.

[5] H. L. Tuller, S. R. Bishop, *Annu. Rev. Mater. Res.* **2011**, *41*, 369.

[6] H. S. Hsu, J. C. a. Huang, Y. H. Huang, Y. F. Liao, M. Z. Lin, C. H. Lee, J. F. Lee, S. F. Chen, L. Y. Lai, C. P. Liu, *Appl. Phys. Lett.* **2006**, *88*, 242507.

[7] J. J. Kim, S. R. Bishop, N. Thompson, D. Chen, H. L. Tuller, *Chem. Mater.* **2014**, *26*, 1374.

[8] E. Boehm, J. Bassat, P. Dordor, F. Mauvy, J. Grenier, P. Stevens, *Solid State Ionics* **2005**, *176*, 2717.

[9] C. Yu, M. L. Scullin, M. Huijben, R. Ramesh, A. Majumdar, *Appl. Phys. Lett.* **2008**, *92*, 191911.

[10] M. N. Luckyanova, D. Chen, W. Ma, H. L. Tuller, G. Chen, B. Yildiz, *Appl. Phys. Lett.* **2014**, *104*, 061911.

[11] D. B. Strukov, G. S. Snider, D. R. Stewart, R. S. Williams, *Nature* **2008**, *453*, 80.

[12] J.-P. Krumme, *Appl. Phys. Lett.* **1973**, *23*, 576.

[13] A. Hagfeldt, G. Boschloo, L. Sun, L. Kloo, H. Pettersson, *Chem. Rev.* **2010**, *110*, 6595.

[14] Y. Min, H. L. Tuller, S. Palzer, J. Wöllenstein, H. Böttner, *Sensors Actuators B Chem.* **2003**, *93*, 435.

[15] C. Branci, N. Benjelloun, J. Sarradin, M. Ribes, *Solid State Ionics* **2000**, *135*, 169.

[16] M. Tsuchiya, B.-K. Lai, S. Ramanathan, *Nat. Nanotechnol.* **2011**, *6*, 282.

[17] J. L. M. Rupp, B. Scherrer, N. Schäuble, L. J. Gauckler, *Adv. Funct. Mater.* **2010**, *20*, 2807.

[18] J. Fleig, F. S. Baumann, V. Brichzin, H. R. Kim, J. Jamnik, G. Cristiani, H. U. Habermeier, J. Maier, *Fuel Cells* **2006**, *6*, 284.

[19] W. Jung, H. L. Tuller, *Solid State Ionics* **2009**, *180*, 843.

[20] S. R. Bishop, T. S. Stefanik, H. L. Tuller, *Phys. Chem. Chem. Phys.* **2011**, *13*, 10165.

[21] E. Baker, M. Iqbal, B. Knox, *J. Mater. Sci.* **1977**, *12*.

[22] H. Takamura, J. Kobayashi, N. Takahashi, M. Okada, *J. Electroceramics* **2008**, *22*, 24.

[23] R. Waser, *J. Am. Ceram. Soc.* **1991**, *40*, 1934.

[24] N. F. Mott, L. Friedman, *Philos. Mag.* **1974**, *30*, 389.

[25] M. Backhaus-Ricoult, K. Adib, T. S. Clair, B. Luerssen, L. Gregoratti, A. Barinov, *Solid State Ionics* **2008**, *179*, 891.

[26] X. J. Chen, S. H. Chan, K. a. Khor, *Electrochem. Solid-State Lett.* **2004**, *7*, A144.

[27] T. Kawada, J. Suzuki, M. Sase, A. Kaimai, K. Yashiro, Y. Nigara, J. Mizusaki, K. Kawamura, H. Yugami, *J. Electrochem. Soc.* **2002**, *149*, E252.

[28] G. J. la O', S.-J. Ahn, E. Crumlin, Y. Orikasa, M. D. Biegalski, H. M. Christen, Y. Shao-Horn, *Angew. Chem. Int. Ed. Engl.* **2010**, *49*, 5344.

[29] BP, *Statistical Review of World Energy 2010.*

[30] J. Larminie, A. Dicks, M. S. McDonald, *Fuel cell systems explained*; Wiley New York, 2003; Vol. 2.

[31] S. M. Haile, *Acta Mater.* **2003**, *51*, 5981.

[32] *Basic Research Needs for the Hydrogen Economy*; 2004.

[33] E. Baur, H. Preis, *Zeitschrift für Elektrochemie und Angew. Phys. Chemie* **1937**, *43*, 727.

[34] E. Ivers-Tiffée, A. Weber, D. Herbstritt, *J. Eur. Ceram. Soc.* **2001**, *21*, 1805.

[35] D. J. L. Brett, A. Atkinson, N. P. Brandon, S. J. Skinner, *Chem. Soc. Rev.* **2008**, *37*, 1568.

[36] J. Richter, P. Holtappels, T. Graule, T. Nakamura, L. J. Gauckler, *Monatshefte für Chemie-Chemical Mon.* **2009**, *140*, 985.

[37] N. Q. Minh, *J. Am. Ceram. Soc.* **1993**, *76*, 563.

[38] M. Mogensen, K. Kammer, *Annu. Rev. Mater. Res.* **2003**, *33*, 321.

[39] W. C. Chueh, S. M. Haile, *Annu. Rev. Chem. Biomol. Eng.* **2012**, *3*, 313.

[40] J. Maier, *Solid State Ionics* **2000**, *135*, 575.

[41] R. Merkle, J. Maier, *Phys. Chem. Chem. Phys.* **2002**, *4*, 4140.

[42] R. a De Souza, *Phys. Chem. Chem. Phys.* **2006**, *8*, 890.

[43] W. Jung, H. L. Tuller, *Adv. Energy Mater.* **2011**, *1*, 1184.

[44] K. A. Gschneidner, L. R. Eyring, G. H. Lander, *Handbook on the Physics and Chemistry of Rare Earths*; Handbook on the Physics and Chemistry of Rare Earths; North-Holland, 2001.

[45] T. H. Etsell, S. N. Flengas, *Chem. Rev.* **1970**, *70*, 339.

[46] S. Bishop, T. Stefanik, H. Tuller, *J. Mater. Res.* **2012**, 1.

[47] Y. L. Yang, C. L. Chen, S. Y. Chen, C. W. Chu, A. J. Jacobson, *J. Electrochem. Soc.* **2000**, *147* , 4001.

[48] F. Lecarpentier, H. Tuller, N. Long, *J. Electroceramics* **2000**, *5*, 225.

[49] B. Steele, *Solid State Ionics* **2000**, *135*, 445.

[50] H. Uchida, N. Mochizuki, M. Watanabe, *J. Electrochem. Soc.* **1996**, *143*, 1700.

[51] P. Shuk, *Solid State Ionics* **1999**, *116*, 217.

[52] X. Qi, Y. S. Lin, C. T. Holt, S. L. Swartz, *J. Mater. Sci.* **2003**, *38*, 1073.

[53] T. Stefanik, H. Tuller, *J. Electroceramics* **2004**, *13*, 771.

[54] M. Nauer, C. Ftikos, B. C. H. Steele, *J. Eur. Ceram. Soc.* **1994**, *14*, 493.

[55] Y. Takasu, T. Sugino, Y. Matsuda, *J. Appl. Electrochem.* **1984**, *14*, 79.

[56] P. Knauth, H. L. Tuller, *J. Eur. Ceram. Soc.* **1999**, *19*, 831.

[57] S. R. Bishop, T. S. Stefanik, H. L. Tuller, *J. Mater. Res.* **2012**, *27*, 2009.

[58] C. Chatzichristodoulou, P. V. Hendriksen, *J. Electrochem. Soc.* **2010**, *157*, B481.

[59] S. R. Bishop, H. L. Tuller, Y. Kuru, B. Yildiz, *J. Eur. Ceram. Soc.* **2011**, *31*, 2351.

[60] Y. Kuru, D. Marrocchelli, S. R. S. Bishop, D. Chen, B. Yildiz, H. L. Tuller, *J. Electrochem. Soc.* **2012**, *159*, F799.

[61] S. R. Bishop, T. S. Stefanik, H. L. Tuller, *J. Mater. Res.* **2012**, *27*, 2009.

[62] S. B. Adler, J. A. Lane, B. C. H. Steele, *J. Electrochem. Soc.* **1996**, *143*, 3554.

[63] V. Dusastre, J. A. Kilner, *Solid State Ionics* **1999**, *126*, 163.

[64] M. J. Jørgensen, M. Mogensen, *J. Electrochem. Soc.* **2001**, *148*, A433.

[65] M. Liu, *J. Electrochem. Soc.* **1998**, *145*, 142.

[66] Z. P. Shao, S. M. Haile, *Nature* **2004**, *431*, 170.

[67] D. B. Chrisey, G. K. Hubler, *Pulsed Laser Deposition of Thin Films*; Wiley, 1994.

[68] W. Jung, A new model describing cathode kinetics in Solid Oxide Fuel Cell: Model Thin Film SrTi1-xFexO3-δ Mixed Conducting Oxides – a case study, Massachusetts Institute of Technology, 2010.

[69] D. Macdonald, *Electrochim. Acta* **2006**.

[70] J. E. Bauerle, J. Hrizo, *J. Phys. Chem. Solids* **1969**, *30*, 565.

[71] W. Lai, S. M. Haile, *J. Am. Ceram. Soc.* **2005**, *88*, 2979.

[72] W. Lai, Impedance Spectroscopy as a Tool for the Electrochemical Study of Mixed Conducting Ceria, Caltech, 2007, Vol. 2007.

[73] G. Reinhardt, V. Baitinger, W. Göpel, *Ionics (Kiel).* **1995**, *1*, 504.

[74] J. Jamnik, J. Maier, *Phys. Chem. Chem. Phys.* **2001**, *3*, 1668.

[75] S. Wang, S. Cho, H. Wang, A. Jacobson, *ECS Trans.* **2011**, *35*, 1891.

[76] T. Nakamura, K. Yashiro, K. Sato, J. Mizusaki, *Solid State Ionics* **2009**, *180*, 368.

[77] W. C. Chueh, S. M. Haile, *Phys. Chem. Chem. Phys.* **2009**, *11*, 8144.

[78] G. T. Kim, S. Wang, A. J. Jacobson, Z. Yuan, C. Chen, *J. Mater. Chem.* **2007**, *17*, 1316.

[79] S. R. Bishop, T. S. Stefanik, H. L. Tuller, *Phys. Chem. Chem. Phys.* **2011**, *13*, 10165.

[80] H. Tuller, A. Nowick, *J. Phys. Chem. Solids* **1977**, *38*, 859.

[81] C. Chatzichristodoulou, P. V. Hendriksen, A. Hagen, *J. Electrochem. Soc.* **2010**, *157*, B299.

[82] T. Nakamura, K. Yashiro, A. Kaimai, T. Otake, K. Sato, T. Kawada, J. Mizusaki, *J. Electrochem. Soc.* **2008**, *155*, B1244.

[83] K. Masato, Y. Masahiro, *Bull. Chem. Soc. Jpn.* **1999**, *72*, 1427.

[84] S. Chapra, R. Canale, *Numerical Methods for Engineers*; McGraw-Hill, Inc., 2005.

[85] S. B. Adler, *Chem. Rev.* **2004**, *104*, 4791.

[86] J. Fleig, *Solid State Ionics* **2002**, *150*, 181.

[87] W. Jung, H. L. Tuller, *J. Electrochem. Soc.* **2008**, *155*, B1194.

[88] E. Thiele, L. Wang, T. Mason, S. Barnett, *J. Vac. Sci. Technol. A Vacuum, Surfaces, Film.* **1991**, *9*, 3054.

[89] P. Manning, J. Sirman, R. De Souza, J. Kilner, *Solid State Ionics* **1997**, *100*, 1.

[90] T. Petrovsky, H. U. Anderson, V. Petrovsky, *Mater. Res. Soc. Symp. Proc.* **2003**, *756*, EE4.7.1.

[91] J. Fleig, H.-R. Kim, J. Jamnik, J. Maier, *Fuel Cells* **2008**, *8*, 330.

[92] S. P. Jiang, *J. Mater. Sci.* **2008**, *43*, 6799.

[93] W. C. Jung, H. L. Tuller, *J. Electrochem. Soc.* **2008**, *155*, 1194.

[94] F. S. Baumann, J. Fleig, G. Cristiani, B. Stuhlhofer, H.-U. Habermeier, J. Maier, *J. Electrochem. Soc.* **2007**, *154*, B931.

[95] M. Y. Sinev, G. Graham, L. Haack, M. Shelef, *J. Mater. Res.* **1996**, *11*, 1960.

[96] N. Imanishi, T. Matsumura, Y. Sumiya, K. Yoshimura, A. Hirano, Y. Takeda, D. Mori, R. Kanno, *Solid State Ionics* **2004**, *174*, 245.

[97] J. Maier, *Physical Chemistry of Ionic Materials*; John Wiley & Sons, Ltd: Chichester, UK, 2004.

[98] B. C. H. Steele, *Solid State Ionics* **1995**, *75*, 157.

[99] T. S. Stefanik, Electrical Properties and Defect Structure of Praseodymium-Cerium Oxide Solid Solutions, Massachusetts Institute of Technology, 2004, Vol. 50, p. 135.

[100] H. Ullmann, *Solid State Ionics* **2000**, *138*, 79.

[101] S. Bishop, K. Duncan, E. Wachsman, *Electrochim. Acta* **2009**, *54*, 1436.

[102] T. Otake, *Solid State Ionics* **2003**, *161*, 181.

[103] D. Chen, S. R. Bishop, H. L. Tuller, *Adv. Funct. Mater.* **2013**, *23*, 2168.

[104] W. Jung, H. L. Tuller, *Energy Environ. Sci.* **2012**, 5370.

[105] G. J. la O', R. F. Savinell, Y. Shao-Horn, *J. Electrochem. Soc.* **2009**, *156*, B771.

[106] W. C. Chueh, Electrochemical & Thermochemical Behavior of CeO2, Caltech, 2011, Vol. 2011.

[107] W. C. Chueh, A. H. McDaniel, M. E. Grass, Y. Hao, N. Jabeen, Z. Liu, S. M. Haile, K. F. McCarty, H. Bluhm, F. El Gabaly, *Chem. Mater.* **2012**, *24*, 1876.

[108] D. Chen, S. R. Bishop, H. L. Tuller, *J. Electroceramics* **2012**, *28*, 62.

[109] U. Bauer, S. Emori, G. S. D. Beach, *Nat. Nanotechnol.* **2013**, *8*, 411.

[110] M. M. Kuklja, E. a. Kotomin, R. Merkle, Y. a. Mastrikov, J. Maier, *Phys. Chem. Chem. Phys.* **2013**, 5443.

[111] L. Wang, R. Merkle, J. Maier, *J. Electrochem. Soc.* **2010**, *157*, B1802.

[112] J. G. Swallow, W. H. Woodford, Y. Chen, Q. Lu, J. J. Kim, D. Chen, Y.-M. Chiang, W. C. Carter, B. Yildiz, H. L. Tuller, K. J. Vliet, *J. Electroceramics* **2014**, *32*, 3.